Optimized explicit schemes: matching and boundary schemes and 4th-order Runge-Kutta algorithm.

Julien Berland,* Christophe Bogey† and Christophe Bailly‡
Laboratoire de Mécanique des Fluides et d'Acoustique
Ecole Centrale de Lyon & UMR CNRS 5509
69134 Ecully, France.

Some numerical tools for local features of the computational domain are built up by minimizing their dispersion and dissipation properties in the Fourier space for low wavenumbers. First, matching schemes are designed. They allow acoustic waves to travel between a uniform Δx-mesh and a 2Δx-mesh. Secondly, non-centered finite difference schemes and selective filters for wall boundary conditions are computed. Time integration is also investigated. An optimized fourth-order six-step Runge-Kutta scheme which remains fourth-order with nonlinear operators is developed. Problems of linear and nonlinear propagation and of wall reflection are finally resolved to illustrate accuracy of the numerical methods designed here.

I. Introduction

Since the earliest stages in computational aeroacoustics, the need for highly accurate schemes has been recognized.[1] Past decade works on numerical methods aimed at designing low dissipative, low dispersive and large spectral bandwidth schemes.[2–5] Methods used in numerical algorithms for spatial and time discretization have thus been optimized by minimizing their dispersion and dissipation properties in the Fourier space for low wavenumbers. Recently, finite-difference schemes, selective filters and explicit Runge-Kutta algorithm[5] were developed in our group to ensure accuracy for waves down to four points per wavelength, allowing direct computation of aerodynamic noise using Large Eddy Simulation.[6,7] However, some numerical tools built up in a similar way are still missing for local features of the computation domain.

First, in aeroacoustic problems the need to take account for both acoustic and aerodynamic length scales usually implies grid stretching. It may be a slow way which might generate numerical errors.[5] The problem is treated here by using a computation domain divided into sub-domains where mesh size is uniform. Tam[8] for instance, developed seven-point cell-centered finite differences and selective filters. In the present work, specific centered schemes which permit resolved waves to travel between a Δx-grid domain and $2\Delta x$-grid domain are designed. Sixth-order seven-point and tenth-order eleven-point matching finite differences and selective filters are proposed.

Secondly, practical implementation of free-field boundary conditions as well as wall boundary conditions usually involves small-stencil schemes which locally lower accuracy. However, to avoid extra-damping and accuracy loss it may be recommended to use non-centered optimized schemes with high accuracy properties. Visbal developed implicit non-centered finite differences[9] and implicit selective filters[10] which enable acoustic and aerodynamic computations for complex geometries.[11,12] Tam[13] also, built up non-centered seven-point explicit optimized finite differences and selective filters

*PhD Student, julien.berland@ec-lyon.fr
†Research scientist CNRS, christophe.bogey@ec-lyon.fr
‡Professor of Ecole Centrale de Lyon, Member AIAA, christophe.bailly@ec-lyon.fr

to implement wall boundary conditions using a ghost point to set normal pressure gradient at the wall to zero. In the present work, non-centered seven- and eleven-point explicit optimized finite differences and selective filters are proposed. They are designed to accurately resolve waves with at least five points per wavelength.

Finally, turbulent flow development and strong acoustic phenomena are driven by nonlinear mechanisms. Available Runge-Kutta algorithms designed for aeroacoustic purposes are usually optimized for integration of linear operators but low-order in nonlinear: for instance, Hu[2] and Bogey[5] proposed second-order six-stage algorithms optimized for linear operators. However one may need a low-storage[14] Runge-Kutta algorithm with higher order in nonlinear to better account for nonlinear phenomena. Stanescu and Habashi[15] gave two fourth-order low-storage Runge-Kutta algorithms. One has low stability properties and the other is a two-level scheme combining two fourth-order Runge-Kutta algorithms. Computational cost is thus significant. Six-stage low-storage Runge-Kutta algorithm of order four in nonlinear, optimized for linear operators and with a wide stability range is therefore proposed here.

In the present paper, matching schemes, boundary schemes and fourth-order six-stage low-storage Runge-Kutta algorithm are presented in Sections II–IV, respectively. At the end of each Section, test cases are resolved to highlight properties of algorithms. Concluding remarks are drawn in Section V.

II. Matching schemes

A. Finite differences

A finite difference formulation appropriate for a non-uniform grid (x_i) is introduced. The local mesh size is defined as the smallest gap between x_i and his first neighbors, i.e.

$$\Delta x_i = \min(x_{i+1} - x_i, x_i - x_{i-1}) \tag{1}$$

Actually, $2\Delta x_i$ is the smallest wavelength that the scheme is able to resolve at the node x_i. The spatial derivative of a function f at x_i is approximated by

$$\left(\frac{\partial f}{\partial x}\right)_i = \frac{1}{\Delta x_i} \sum_{j=-N}^{N} a_j f(x_{i+j}) \tag{2}$$

In the present work, coefficients a_j are determined to cancel the terms of the Taylor series of (2) so that the maximum order of accuracy is reached. For $i \neq j$ we have

$$f(x_{i+j}) = \sum_{p=0}^{2N} \frac{\beta_{ij}^p {\Delta x_i}^p}{p!} f^{(p)}(x_i) + \mathcal{O}({\Delta x_i}^{2N+1}) \tag{3}$$

where $\beta_{ij} = (x_{i+j} - x_i)/\Delta x_i$. Thus, according to (2)

$$\left(\frac{\partial f}{\partial x}\right)_i = \frac{f(x_i)}{\Delta x_i} \sum_{j=-N}^{N} a_j + \sum_{p=1}^{2N} \sum_{\substack{j=-N \\ j\neq 0}}^{N} a_j \frac{\beta_{ij}^p {\Delta x_i}^{p-1}}{k!} f^{(p)}(x_i) + \mathcal{O}({\Delta x_i}^{2N}) \tag{4}$$

To obtain an order of accuracy $2N$, the coefficients a_j are solutions of the following system of equations

$$\begin{cases} \displaystyle\sum_{j=-N}^{N} a_j = 0 \\ \displaystyle\sum_{\substack{j=-N \\ j\neq 0}}^{N} a_j \beta_{ij}^p = \delta_{p1}, \qquad p = 1, \ldots, 2N \end{cases} \tag{5}$$

In the present work sixth-order seven-point and tenth-order eleven-point finite difference schemes have been designed thanks to (5) for buffer region between uniform Δx–mesh and uniform $2\Delta x$–mesh as shown in Figure 1. Coefficients are given in Table 6 and Table 7. Scheme names are defined in Figure 2: subscript is the number of points and exponent is the point number where the transition occurs. For brevity, seven-point schemes will not be described here as they have similar properties to the eleven-point schemes.

Dispersion and dissipation properties of the finite difference schemes are determined by applying spatial Fourier transform to equation (2). The effective (complex) wavenumber k^* of the scheme is then given by

$$k^*\Delta x_i = -i\sum_{j=-N}^{N} a_j e^{i\beta_{ij}k\Delta x_i} \tag{6}$$

To illustrate the scheme properties, consider the convective equation where approximated derivative $\delta/\delta x$ is processed with (2):

$$\frac{\partial u}{\partial t} + c\frac{\delta u}{\delta x} = 0 \tag{7}$$

Dispersion relation is

$$\omega = k^* c \tag{8}$$

Take a left-running harmonic wave $u(x, t = 0) = e^{ikx}$ as initial disturbance. The solution is

$$u(x,t) = e^{i(kx-\omega t)} \tag{9}$$

According to (8) it may be rewritten as

$$u(x,t) = e^{i(kx-k^*ct)} = \underbrace{e^{i[k-\mathcal{R}e(k^*)]ct}}_{\text{dispersion}} \cdot \underbrace{e^{\mathcal{I}m(k^*)ct}}_{\text{dissipation}} \cdot \underbrace{e^{ik(x-ct)}}_{\substack{\text{exact}\\ \text{factor}}} \tag{10}$$

Thus, dispersion error is $k^*\Delta x_i - \mathcal{R}e(k^*\Delta x_i)$, and amplitude of the wave is multiplied by $e^{\mathcal{I}m(k^*\Delta x_i)}$ for a left-running wave and by $e^{-\mathcal{I}m(k^*\Delta x_i)}$ for a right-running wave.

The error between the effective and the exact wavenumber $|\mathcal{R}e(k^*\Delta x_i) - k\Delta x|/\pi$ is plotted for the eleven-point schemes in Figure 3 for the Δx-schemes ($\Delta x_i = \Delta x$) and in Figure 4 for the $2\Delta x$-schemes ($\Delta x_i = 2\Delta x$) as a function of $k\Delta x$, in logarithmic scales. Centered standard tenth-order eleven-point scheme is also plotted for comparison. It is referred to as $\text{FD}_{55}^{\text{s}}$. Remark that the cut-off wavenumber of the $2\Delta x$-schemes is $k_c\Delta x = \pi/2$. Indeed, grid-to-grid oscillations corresponding to a two-point-per-wavelength wave on a $2\Delta x$-mesh correspond to a four-point-per-wavelength wave on a Δx-mesh.

Note that the dispersion error remains lower than 5×10^{-3} up to about $k\Delta x < \pi/2$ for all the Δx-schemes and $k\Delta x < \pi/4$ for all the $2\Delta x$-schemes. These limits in wavenumber respectively correspond to four and eight points per wavelength with respect to the Δx-mesh. Grid-to-grid waves ($k\Delta x = \pi$ on Δx-mesh and $k\Delta x = \pi/2$ on $2\Delta x$-mesh) are never resolved.

The amplification factor $e^{\pm\mathcal{I}m(k^*\Delta x_i)}$ for the eleven-point schemes is also plotted in Figure 3 for the Δx-schemes and in Figure 4 for the $2\Delta x$-schemes as a function of $k\Delta x$, in logarithmic scales. For low wavenumbers, i.e. about $k\Delta x < \pi/2$ for Δx-schemes and $k\Delta x < \pi/4$ for $2\Delta x$-schemes, amplification factors remain close to 1. For higher wavenumbers, especially grid-to-grid oscillations, the amplification factor is such as $e^{\mathcal{I}m(k^*\Delta x_i)} > 1$ and $e^{-\mathcal{I}m(k^*\Delta x_i)} < 1$. Left-running waves are therefore amplified and right-running waves are damped. These non-resolved waves are to be removed by selective filters.

For quantitative comparisons, limits of accuracy in phase and amplitude are respectively assessed through the criteria $|\mathcal{R}e(k^*\Delta x_i) - k\Delta x_i|/\pi < 5\times10^{-3}$ and $|1 - e^{\mathcal{I}m(k^*\Delta x_i)}| < 5\times10^{-3}$ which represent half a percent error. These quantities are reported in Table 1. Remark that limit wavenumbers and limit wavelengths are given with respect to the Δx-mesh. Limits of accuracy of the centered standard tenth-order eleven-point finite differences are also given on both grids. Limit of accuracy in phase of the centered scheme shows that it resolves accurately at least four-point-per-wavelength waves on the Δx-mesh and waves with eight points per wavelength in the $2\Delta x$-mesh. As for the centered scheme,

limit of accuracy in phase of the Δx-schemes is about four points per wavelength and about eight points per wavelength for the $2\Delta x$-schemes. Dissipation limit is also about four points per wavelength for the Δx-schemes and about eight points per wavelength for the $2\Delta x$-schemes.

These limits of accuracy demonstrate that matching finite differences permit waves discretized by eight points per wavelength in the Δx-mesh to travel inside the buffer region. Four points per wavelength waves in the $2\Delta x$-mesh are then accurately resolved when they travel from a mesh region to another. Smaller wavelengths, i.e. waves with less than four points per wavelength in the $2\Delta x$-mesh, are not well resolved by the $2\Delta x$-schemes. Thus they must be removed by selective filtering.

B. Selective filters

To remove grid-to-grid oscillations, selective filtering of a function f is performed by the scheme

$$f^d(x_i) = f(x_i) - \sigma \sum_{j=-N}^{N} d_j f(x_{i+j}) \tag{11}$$

where f^d is the filtered function, d_j are the stencil coefficients and σ is a constant taken between 0 and 1 defining filtering strength. Consider the spatial Fourier transform of (11) to compute the frequency response function of the filter

$$G(k\Delta x_i) = 1 - \sigma \sum_{j=-N}^{N} d_j e^{i\beta_{ij} k\Delta x_i} \tag{12}$$

with the Δx_i and β_{ij} defined in Section A. To determine the coefficients d_j, terms resulting from the Taylor series of (12) obtained as $k\Delta x_i \to 0$ are canceled. We may write

$$G(k\Delta x_i) = 1 - \sigma \left[\sum_{j=-N}^{N} d_j \right] - \sigma \sum_{p=1}^{2N-1} \frac{(ik\Delta x_i)^p}{p!} \left[\sum_{j=-N}^{N} \beta_{ij}^p d_j \right] + \mathcal{O}(k\Delta {x_i}^{2N}) \tag{13}$$

Enforcing also the two following criteria

$$\begin{aligned} G(0) &= 1 + \mathcal{O}(k\Delta {x_i}^{2N}) \\ G(\pi) &= 1 - \sigma \end{aligned} \tag{14}$$

gives a system of equations to determine the d_j coefficients:

$$\begin{cases} \displaystyle\sum_{j=-N}^{N} (-1)^j d_j = 1 \\ \displaystyle\sum_{j=-N}^{N} d_j = 0 \\ \displaystyle\sum_{j=-N}^{N} d_j \beta_{ij}^p = 0, \qquad p = 1, \ldots, 2N-1 \end{cases} \tag{15}$$

Sixth-order seven-point and tenth-order eleven-point matching selective filters between Δx and $2\Delta x$-meshes have been built up. Their coefficients are given in Table 8 and Table 9. Stencil names are defined as in Section A. Note that coefficient d_5 of SF_{11}^{0} has been optimized so that the filter remains stable with $G(k\Delta x_i) < 1$ for $k\Delta x_i$ in $[0, \pi]$. Setting one coefficient free is made possible by reducing filter order of accuracy to nine. Seven-point filters are not described here as they have similar properties to the eleven-point schemes.

In order to investigate filter properties in the Fourier space, the frequency response function is written as

$$G(k\Delta x_i) = |G| e^{i\phi(G)} \tag{16}$$

where $|G|$ is the module and $\phi(G)$ denotes the argument of G. Amount of dissipation $1-|G(k\Delta x_i)|$ and phase error $|\phi(G(k\Delta x_i))|/\pi$ are plotted for the eleven-point schemes in Figure 5 for the Δx-filters ($\Delta x_i = \Delta x$) and in Figure 6 for the $2\Delta x$-filters ($\Delta x_i = 2\Delta x$) as functions of $k\Delta x$, in logarithmic scales. It is compared to the tenth-order eleven-point standard centered selective filter. Amount of dissipation of the Δx- and $2\Delta x$-filters is closed to the amount of dissipation of the centered filter. As expected, dissipation is small for low wavenumbers. It is lower than 5×10^{-3} up to $k\Delta x < \pi/2.5$ for Δx-filters and up to $k\Delta x < \pi/5$ for $2\Delta x$-filters. These limits in wavenumber correspond to five-point-per-wavelength waves on the Δx-mesh and to waves with ten points per wavelength on the $2\Delta x$-mesh. As expected, dissipation is significant for grid-to-grid oscillations.

Phase error is lower than 5×10^{-3} up to about $k\Delta x < \pi/2.5$ for Δx-filters and up to $k\Delta x < \pi/5$ for $2\Delta x$-filters, i.e. down to five and ten points per wavelength on the Δx- and the $2\Delta x$-mesh. For high wavenumbers, $k\Delta x \sim \pi$ for Δx-filters and $k\Delta x \sim \pi/2$ for $2\Delta x$-filters, phase error becomes significant but these waves are filtered out.

To quantitatively compare the filter properties, limits in dissipation and phase error are estimated from the criteria based on half a percent error: $1-|G(k\Delta x_i)| < 5\times10^{-3}$ and $|\phi(G(k\Delta x_i))|/\pi < 5\times10^{-3}$. Results are reported in Table 2 in wavenumbers and wavelengths with respect to the Δx-mesh. Centered tenth-order eleven-point selective filter dissipation limit is also reported: dissipation limit is about five points per wavelength on the Δx-mesh and ten points per wavelength on the $2\Delta x$-mesh. Matching filters have a similar amount of dissipation. Indeed, dissipation limit is about five points per wavelength for Δx-filters and ten points per wavelength for $2\Delta x$-filters. Phase error limits are also about five points per wavelength for Δx-filters and ten points per wavelength for $2\Delta x$-filters.

The dissipation and phase errors show that matching filters remove waves with less than ten points per wavelength in the Δx-mesh. As a result, five-point-per-wavelength waves and larger wavelengths are not filtered out when they pass through the buffer region. Smaller wavelengths, discretized by less than five points in the $2\Delta x$-mesh, are removed by the filters.

C. Test problems

Properties of the matching schemes have been first illustrated by solving the convective wave equation

$$\frac{\partial u}{\partial t} + \epsilon\frac{\partial u}{\partial x} = 0 \tag{17}$$

where $\epsilon = 1$ for right-running waves and $\epsilon = -1$ for left-running waves. The grid is non-uniform: at $x = 0$ the mesh size changes from Δx to $2\Delta x$ as shown in Figure 7. Initial disturbances at $t = 0$ are defined as

$$u_0(x) = \cos\left[\frac{2\pi}{a\Delta x}(x-x_0)\right]\exp\left[-\ln(2)\left(\frac{x-x_0}{b\Delta x}\right)^2\right] \tag{18}$$

where $a\Delta x$ is the dominant wavelength, $b\Delta x$ is the half-width of the Gaussian function and x_0 is the starting point of the wave. The aim is to study waves with five points per wavelength in the coarse mesh. Parameters are thus set to:

1. right-running wave: $\epsilon = 1$, $a = 10$, $b = 12$, $x_0 = -30$;
2. left-running wave: $\epsilon = -1$, $a = 10$, $b = 12$, $x_0 = 30$.

Dominant wavelength corresponds to a ten-point-per-wavelength wave in the Δx-mesh and to a five-point-per-wavelength wave in the $2\Delta x$-mesh. Half-width of the Gaussian is chosen so that spectral content of the initial perturbation does not contain waves with less than four points per wavelength. The solution is computed up to $t = 60$. Optimized six-stage Runge-Kutta algorithm developed by Bogey[5] is used for time integration with a CFL $= \Delta t/\Delta x$ number equals to 0.8. Eleven-point optimized finite differences and selective filtering[5] are implemented to discretize the problem for the regions of uniform grid. These algorithms permit to resolve waves with at least four points per wavelength. Matching eleven-point finite differences and selective filters are applied to buffer regions between uniform mesh sub-domains. Initial perturbations and solutions computed at $t = 60$ are plotted in

Figures 8 and 9 for respectively right- and left-running waves. No notable dissipation or dispersion is seen to be generated when the wave goes through the buffer region. Indeed, after the buffer region, wave shape perfectly fits the exact solution for both direction of propagation.

A second test case involves the two-dimensional Navier-Stokes equations. The local mesh size is given by

$$\Delta x_i = \begin{cases} \Delta x & \text{if} \quad |x/\Delta x| \leq 15 \\ 2\Delta x & \text{if} \quad 15 < x/\Delta x \leq 75 \text{ or } -75 \leq x/\Delta x < -15 \\ 4\Delta x & \text{if} \quad |x/\Delta x| > 75 \end{cases} \tag{19}$$

and $\Delta y_i = \Delta x$. Number of points is 161×101. Optimized six-stage Runge-Kutta algorithm, eleven-point optimized finite differences and selective filtering developed by Bogey[5] are used. CFL number is 2/3. The equations are solved in dimensional forms.

An acoustic source is considered at the center of the domain. The following source term is added to the right-hand side of the Navier-Stokes equations:

$$S(x, y, t) = A\omega \sin(\omega t) \exp\left[-\frac{\ln(2)}{4}(x^2 + y^2)\right] \tag{20}$$

where $A = 250$ and $\omega = 2\pi c_0 \,/\, 20\Delta x$. Acoustic wavelength is then discretized by 20 points in the Δx–mesh region, and by 5 points in the $4\Delta x$–mesh region. The computed pressure for $x \geq 0$ with a schematic view of the different mesh regions is plotted in Figure 10. Wave fronts are continuous, no significant dissipation or dispersion is observed at the buffer regions. Pressure distribution along the line $y = 0$ is plotted in Figure 11. It is compared to the solution computed on a uniform Δx–mesh: the two pressure distributions agree over the whole line. Buffer regions do not introduce any significant local errors at $x = 15$ or $x = 75$.

The behavior of the matching schemes is now investigated for an aerodynamic problem. Consider the convection of a vortex in a uniform flow $\overline{\mathbf{u}} = (0.3c_0, 0)$. The mesh is non-uniform in the x-direction. The local mesh size Δx_i is defined as follow:

$$\Delta x_i = \begin{cases} \Delta x & \text{if} \quad |x/\Delta x| \leq 15 \\ 2\Delta x & \text{if} \quad |x/\Delta x| > 15 \end{cases} \tag{21}$$

and $\Delta y_i = \Delta x$. Problem is discretized using the algorithms of Bogey[5] as above. CFL number is 2/3. The vortex, initially at the position $(x_0, y_0) = (-115, 0)$, is defined by the velocity distribution:

$$\begin{aligned} u_x &= \overline{u} + \epsilon \frac{y - y_0}{\Delta x} \exp\left[-\alpha(x - x_0)^2 - \alpha(y - y_0)^2\right] \\ u_y &= -\epsilon \frac{x - x_0}{\Delta x} \exp\left[-\alpha(x - x_0)^2 - \alpha(y - y_0)^2\right] \end{aligned} \tag{22}$$

where $\alpha = \ln(2)/25\Delta x^2$ and $\epsilon = 10$. Pressure perturbations associated to the vortex are about 1000 Pa. The vortex comes from the left part of the computation domain and passes through the finer mesh area. The computed solution is plotted in Figure 12 for various time steps. Remark that residual pressure is generated when the vortex hits the two buffer regions. Amplitude is about 1 Pa, i.e. one per mille of the incident pressure perturbation. The reflection rate of aerodynamic pressure is thus low. For acoustic purposes however, a great care is to be taken to ensure that reflected waves do not overwhelm acoustic pressure, especially for flows at low Mach numbers.

III. Boundary schemes

A. Finite differences

The spatial derivative of a function f can be approximated on a uniform grid (x_i) using a non-centered finite difference scheme by

$$\left(\frac{\partial f}{\partial x}\right)_i = \frac{1}{\Delta x} \sum_{j=-P}^{Q} a_j f(x_i + j\Delta x) \tag{23}$$

where Δx is the mesh size and a_j are stencil coefficients. The approximation uses P points left to x_i and Q points right to x_i. Applying spatial Fourier transform to (23) yields the effective wavenumber k^* of the scheme

$$k^*\Delta x = -i \sum_{j=-P}^{Q} a_j e^{ijk\Delta x} \tag{24}$$

In this work, following Tam and Webb[4] for instance, coefficients a_j are determined to minimize dispersion and dissipation of the scheme. To ensure a minimum order of accuracy the terms of the Taylor series of (23) are canceled up to the fourth order. Coefficients a_j are then determined to minimize the integral error defined by

$$\int_{\pi/16}^{\pi/2} \Big[(1-\alpha)|\mathcal{R}e(k^*\Delta x) - k\Delta x| + \alpha|\mathcal{I}m(k^*\Delta x)|\Big] \frac{d(k\Delta x)}{k\Delta x} \tag{25}$$

where $0 < \alpha < 0.5$ according to the scheme. Bounds of the integral are chosen to put emphasis during the optimization on waves between 32 points per wavelength ($k\Delta x = \pi/16$) and 4 points per wavelength ($k\Delta x = \pi/2$). Fourth order seven- and eleven-point non-centered finite difference schemes have been designed by this way. Coefficients are given in Table 10 and Table 11. Scheme names are defined as FD_{PQ} as shown in Figure 13. Seven-point schemes are not described here as they have similar properties to the eleven-point schemes.

Dispersion and dissipation properties of the eleven-point schemes are plotted in Figure 15 as functions of $k\Delta x$, in logarithmic scales. Eleven-point centered optimized finite difference scheme built in a similar way by Bogey[5] is also plotted. It is referred to as FD_{55}. Dispersion error $|k^*\Delta x - k\Delta x|/\pi$ remains closed to that of the centered scheme for all the non-centered schemes. Non-centered schemes dispersion error is lower than 5×10^{-3} up to about $k\Delta x = \pi/2.5$, i.e. five points per wavelength.

For wavenumbers lower than $k\Delta x = \pi/2.5$, amplification factor $e^{\pm\mathcal{I}m(k^*\Delta x)}$ nearly equals 1 and thus wave amplitude is not modified. To the contrary, grid-to-grid oscillations with $k\Delta x = \pi$ are damped or amplified. Indeed, close to $k\Delta x = \pi$, $e^{\mathcal{I}m(k^*\Delta x)} > 1$ and $e^{-\mathcal{I}m(k^*\Delta x)} < 1$, i.e. left-running waves are amplified and right-running waves are damped.

Criteria of accuracy based on half a percent error are introduced to assess the schemes, $|\mathcal{R}e(k^*\Delta x) - k\Delta x|/\pi < 5\times10^{-3}$ and $|1-e^{\mathcal{I}m(k^*\Delta x)}| < 5\times10^{-3}$, for respectively dispersion and dissipation. Accuracy limits are given in Table 3. Centered optimized finite difference scheme is added for comparison. Dispersion accuracy limit is about four points per wavelength for the centered scheme. Non-centered schemes FD_{46}, FD_{37} and FD_{28} also have a dispersion limit close to four points per wavelength. Schemes FD_{19} and FD_{010}, which are more asymmetric, are more dispersive: their dispersion limits are about five points per wavelength. In addition, dissipation limits are about five points per wavelength for all the non-centered schemes.

The investigation of dispersion and dissipation accuracy limits demonstrates that non-centered finite differences accurately resolve waves with at least five points per wavelength. Non-resolved smaller wavelengths, which may lead to instabilities when they are amplified, must be removed by selective filtering.

B. Selective filters

Non-centered selective filtering of a function f is processed such as

$$f^d(x) = f(x) - \sigma \sum_{j=-P}^{Q} d_j f(x + j\Delta x) \tag{26}$$

where f^d is the filtered function, Δx is the mesh size, d_j are the coefficients of the scheme, and σ is a constant taken between 0 and 1 defining filtering strength. Consider the spatial Fourier transform of (26) to compute the frequency response function of the filter:

$$G(k\Delta x) = 1 - \sigma \sum_{j=-P}^{Q} d_j e^{ijk\Delta x} \tag{27}$$

The filter is second order, i.e. $G(0) = 1 + \mathcal{O}(k\Delta x^2)$ and $G(\pi) = 1 - \sigma$. Coefficients are then optimized in the spectral space by minimizing the integral error

$$\int_{\pi/16}^{\pi/2} \left[(1-\alpha)|G(k\Delta x)| + \alpha|\phi(G(k\Delta x)|\right] \frac{d(k\Delta x)}{k\Delta x} \tag{28}$$

where $0 < \alpha < 0.01$ according to the filters and $\phi(G)$ is the argument of the frequency response function. Integral is made over the interval corresponding to the wavenumbers to be optimized, $k\Delta x$ in $[\pi/16, \pi/2]$, corresponding to waves with 32 points per wavelength to 4 points per wavelength. In this work second-order seven- and eleven-point optimized non-centered selective filters have been designed. Coefficients are given in Table 12 and Table 13 and filter names are defined as finite difference names, i.e. SF_{PQ}. Completely off-centered SF_{010} or SF_{06} have not been provided because they are highly dissipative. Besides, optimization failed to yield a suitable SF_{19} filter. Seven-point filter SF_{15} is therefore used instead of SF_{19}.

The amount of dissipation $1-|G(k\Delta x)|$ and phase error $|\phi(G(k\Delta x))|$ of the eleven-point filters are plotted in Figure 16 in logarithmic scales. Seven-point filter SF_{15} is added but seven-point filter SF_{24} is not described here since it has similar properties to the eleven-point filter SF_{28}. For comparison, tenth-order eleven-point centered optimized selective filter of Bogey[5] is also plotted. As expected, low wavenumbers are not significantly damped. The amount of dissipation of non-centered filters is lower than 5×10^{-3} up to about $k\Delta x = \pi/2.5$, for five points per wavelength. The seven-point filter SF_{15} is more dissipative than the other non-centered filters, especially for wavenumbers between $\pi/16$ and $\pi/4$. Nevertheless, the amount of dissipation remains below 5×10^{-3} for these wavenumbers. For all the filters, the amount of dissipation is significant for waves with $k\Delta x \sim \pi$ in order to remove grid-to-grid oscillations. Phase error is also plotted in Figure 16. Error is lower than 5×10^{-3} up to about $k\Delta x < \pi/2.5$, i.e. down to five points per wavelength. For high wavenumbers, $k\Delta x \sim \pi$, phase error becomes significant but these waves are damped.

The results are quantitatively reported in Table 4. Limits of dissipation and error in phase are estimated using the criteria $|1 - G(k\Delta x)| < 5 \times 10^{-3}$ and $|\phi(G(k\Delta x))|/\pi < 5 \times 10^{-3}$. Damping limits are about four points per wavelength for SF_{46} and SF_{15}. Filter SF_{28} has a damping limit close to five points per wavelength, whereas SF_{37} is slightly more dissipative with a dissipation limit of about six points per wavelength. Phase error limit is about five points per wavelength for filters SF_{37} and SF_{28}, six points per wavelength for SF_{46} and seven points per wavelength for SF_{15}.

The accuracy limits show that non-centered filters remove waves with less than five points per wavelength. Phase error investigation points out that small dispersion is added for waves between six and seven points per wavelength by the filters SF_{46} and SF_{15}. However, this dispersion error is introduced at only two mesh points. Overall accuracy limit may thus be set to five points per wavelength. This limit agrees with the limit of accuracy of the non-centered finite differences.

C. Test problems

A linear acoustic problem is considered in dimensionless form with:

$$\begin{aligned} \frac{\partial u}{\partial t} + \frac{\partial p}{\partial x} &= 0 \\ \frac{\partial p}{\partial t} + \frac{\partial u}{\partial x} &= 0 \end{aligned} \tag{29}$$

Wall boundary conditions are enforced at the boundaries of the computation domain, i.e.

$$\frac{\partial p}{\partial x} = 0, \quad \text{at } x = \pm L \tag{30}$$

Numerically, $\partial p/\partial x$ is set to zero at the boundaries and $\partial u/\partial x$ is computed using the interior points.

An initial disturbance is defined as

$$\begin{cases} u = 0 \\ p = \cos\left(\dfrac{2\pi x}{a\Delta x}\right) \exp\left[-\ln(2)\left(\dfrac{x}{b\Delta x}\right)^2\right] \end{cases} \tag{31}$$

with $a = 6$ and $b = 12$. It is plotted with its power spectral density in Figure 17. Initial perturbation is a wave packet centered on a wave discretized with six points per wavelength. Time integration is processed with an optimized six-stage Runge-Kutta algorithm[5] and the eleven-point optimized finite differences and selective filtering of Bogey[5] are used for centered spatial derivatives. CFL number is set to 0.8. Wall boundary conditions are enforced at $x/\Delta x = \pm 50$. Equations 29 have been solved up to $t = 200$, i.e. after two reflections of the initial wave. Two filtering strength, $\sigma = 0.2$ and $\sigma = 0.8$, applied to both centered and non-centered filters, and three stencil configurations have been tested for the boundaries treatment:

1. centered finite differences and centered selective filters;
2. non-centered optimized finite differences and centered selective filters;
3. non-centered optimized finite differences and non-centered optimized selective filters.

Centered finite differences and filters are standard schemes whose coefficients are computed by maximizing the order of accuracy. One may refer to Figure 14 for centered scheme stencils and to Tables 14 and 15 for coefficients and order of accuracy of the finite differences and selective filters. Solutions of the test case are reported in Figure 18. Figures 18.1a and 18.1b show that waves are nearly completely damped using centered finite differences and centered filters. In Figure 18.2a, when centered finite differences are replaced by non-centered optimized finite differences, dissipation is less important and the shape of the disturbance is kept. However, as filtering strength is increased in Figure 18.2b, the perturbation is significantly damped due to the large amount of dissipation of centered filters. For instance, at $k\Delta x = \pi/3$, the amount of dissipation of SF_{11} is about 0.25, whereas it is about 0.0005 for the non-centered filter SF_{19}. With the use of the non-centered optimized filters, filtering strength has thus little influence on resolved wavenumbers. It is illustrated by Figures 18.3a and 18.3b: increasing filtering strength from $\sigma = 0.2$ to $\sigma = 0.8$ adds some dispersion due to phase errors but the overall amplitude is preserved.

IV. Low-storage 4th-order six-stage Runge-Kutta algorithm

A. Runge-Kutta algorithms

Consider the time integration using Runge-Kutta algorithms of the following differential equation:

$$\frac{\partial u}{\partial t} = F(u,t) \tag{32}$$

where the operator F is a function of the unknown u and of time t. The general formulation of an explicit, p-th order of accuracy, s-stage Runge-Kutta (RK) method for computing the numerical approximation of $u^n = u(t)$ to $u^{n+1} = u(t + \Delta t)$ is

$$\begin{aligned} u^{n+1} &= u^n + \Delta t \sum_{i=1}^{s} b_i k_i \\ k_i &= F\left(t + c_i \Delta t, u^n + \Delta t \sum_{j=1}^{i-1} a_{ij} k_j \right) \end{aligned} \tag{33}$$

where Δt is the time step, b_i and a_{ij} are the coefficients of the algorithm and $c_i = \sum_{j=1}^{i-1} a_{ij}$ for. To ensure an explicit scheme $a_{ij} = 0$ for $i \geq j$.

Several formulations of RK schemes have been built up to improve accuracy and to reduce storage requirements.[2,5,15] Williamson's[14] formulation, which only requires two storage locations per variable, is used here. The algorithm (33) becomes

$$\begin{aligned} \omega_i &= \alpha_i \omega_{i-1} + \Delta t F(u_{i-1}, t_i) \\ u_i &= u_{i-1} + \beta_i \omega_i \quad ; \qquad i = 1, \ldots, s \end{aligned} \tag{34}$$

where $u_0 = u^n$, $u^{n+1} = u_s$ and $t_i = t^{n-1} + \Delta t c_i$. α_i and β_i are the coefficients of the algorithm. To ensure an explicit scheme, α_1 is set to zero.

The present work focuses on an explicit fourth-order six-stage RK scheme referred to as RK46–Ber. The relationships between the usual and the low-storage RK coefficients are found to be[15]:

$$\begin{array}{lcllcl}
a_{65} &=& \beta_5 & a_{41} &=& \alpha_2 a_{42} + \beta_1 \\
a_{64} &=& \alpha_5 a_{65} + \beta_4 & a_{32} &=& \beta_2 \\
a_{63} &=& \alpha_4 a_{64} + \beta_3 & a_{31} &=& \alpha_2 a_{32} + \beta_1 \\
a_{62} &=& \alpha_3 a_{63} + \beta_2 & a_{21} &=& \beta_1 \\
a_{61} &=& \alpha_2 a_{62} + \beta_1 & b_6 &=& \beta_6 \\
a_{54} &=& \beta_4 & b_5 &=& \alpha_6 b_6 + \beta_5 \\
a_{53} &=& \alpha_4 a_{54} + \beta_3 & b_4 &=& \alpha_5 b_5 + \beta_4 \\
a_{52} &=& \alpha_3 a_{53} + \beta_2 & b_3 &=& \alpha_4 b_4 + \beta_3 \\
a_{51} &=& \alpha_2 a_{52} + \beta_1 & b_2 &=& \alpha_3 b_3 + \beta_2 \\
a_{43} &=& \beta_3 & b_1 &=& \alpha_2 b_2 + \beta_1 \\
a_{42} &=& \alpha_3 a_{43} + \beta_2 & & &
\end{array} \tag{35}$$

The aim is now to find a set of equations for the coefficients $(\alpha_2, \ldots, \alpha_6, \beta_1, \ldots, \beta_6)$ which leads to a fourth-order RK scheme, optimized for linear operators and remaining of fourth order for nonlinear operators.

B. Order of accuracy

To have the required order of accuracy, the coefficients must obey order conditions. These are obtained by equating coefficients of the Taylor series of (33). For a fourth-order RK these conditions are[15]

$$\begin{array}{llll}
\text{(O1).i} & \sum b_i = 1 & \text{(O4).i} & \sum b_i c_i^3 = \frac{1}{4} \\
\text{(O2).ii} & \sum b_i c_i = \frac{1}{2} & \text{(O4).ii} & \sum b_i c_i a_{ij} c_j = \frac{1}{8} \\
\text{(O3).i} & \sum b_i c_i^2 = \frac{1}{3} & \text{(O4).iii} & \sum b_i a_{ij} c_j^2 = \frac{1}{12} \\
\text{(O3).ii} & \sum b_i a_{ij} c_j = \frac{1}{6} & \text{(O4).iv} & \sum b_i a_{ij} a_{jk} c_k = \frac{1}{24}
\end{array} \tag{36}$$

where all subscripts extend from 1 to s. On the left of each equation is written the corresponding order of accuracy. Thanks to (35) these relationships may be written as functions of $(\alpha_2, \ldots, \alpha_6, \beta_1, \ldots, \beta_6)$. Eight equations are thus found for the eleven coefficients $(\alpha_2, \ldots, \alpha_6, \beta_1, \ldots, \beta_6)$.

C. Linear optimization

Now assume F is a linear operator which does not depend on the time variable t. The RK scheme (34) may be simplified as

$$u^{n+1} = u^n + \sum_{j=1}^{p} \gamma_j \Delta t^j F^j(u) \tag{37}$$

where $F^j = \underbrace{F \circ \ldots \circ F}_{j}$ and γ_j are the algorithm coefficients. According to (32), we then have

$$u^{n+1} = u^n + \sum_{j=1}^{p} \gamma_j \Delta t^j \frac{\partial^j u^n}{\partial t^j} \tag{38}$$

For a six-stage RK, the coefficients γ_j are given by

$$\begin{array}{lcllcl}
\gamma_1 &=& \sum b_i & \gamma_4 &=& \sum b_i a_{ij} a_{jk} c_k \\
\gamma_2 &=& \sum b_i c_i & \gamma_5 &=& \sum b_i a_{ij} a_{jk} a_{kl} c_l \\
\gamma_3 &=& \sum b_i a_{ij} c_j & \gamma_6 &=& \sum b_i a_{ij} a_{jk} a_{kl} a_{lm} c_m
\end{array} \tag{39}$$

and are therefore functions of $(\alpha_2, \ldots, \alpha_6, \beta_1, \ldots, \beta_6)$.

Following the works of Bogey,[5] the algorithm (38) is constructed by optimizing its dispersion and dissipation properties. Applying temporal Fourier transform to (38) gives the amplification factor of the algorithm:

$$G(\omega\Delta t) = \frac{\hat{u}^{n+1}(\omega)}{\hat{u}^{n}(\omega)} = 1 + \sum_{j=1}^{p} \gamma_j (i\omega\Delta t)^j \tag{40}$$

For comparison with the exact amplification factor $e^{i\omega\Delta t}$, it is written as $|G(\omega\Delta t)|e^{i\omega^*\Delta t}$. At each time step for an angular frequency ω, the amount of dissipation is $1 - |G(\omega\Delta t)|$ and the phase error $\omega\Delta t - \omega^*\Delta t$.

A fourth-order six-stage algorithm has been built. To ensure fourth order we have

$$\gamma_j = \frac{1}{j!} \quad ; \qquad j = 1, \ldots, 4 \tag{41}$$

The two remaining coefficients γ_5 and γ_6 are computed by optimizing the dissipation and dispersion errors up to the angular frequency $\omega\Delta t = \pi/2$. The following integral error is minimized:

$$\int_{\pi/16}^{\pi/2} \left[1 - |G(\omega\Delta t)| + \frac{|\omega\Delta t - \omega^*\Delta t|}{\pi} \right] \frac{d(\omega\Delta t)}{\omega\Delta t} \tag{42}$$

with the conditions

$$\begin{aligned} &|1 - G(\omega\Delta t)| > 0 \\ &\frac{d\ln(1-|G|)}{d(\omega\Delta t)} \geq -5 \end{aligned} \tag{43}$$

for $0 \leq \omega\Delta t \leq \pi$, to ensure stability and to limit the variations of the amplification rate $|G(\omega\Delta t)|$. Bounds of the integral are set to focus on the interval $\omega\Delta t \in [\pi/16, \pi/2]$, for waves between 32 and 4 time steps per period, $T/\Delta t = 2\pi/\omega\Delta t$. Coefficients γ_j are provided in Table 16. The corresponding RK algorithm is referred to as RK46–Ber.

To check stability the amplification rate $|G(\omega\Delta t)|$ is plotted in Figure 19 for the classical fourth-order four-stage RK scheme (RK44), the fourth-order six-stage RK developed by Stanescu and Habashi[15] (RK46–Sta), the second-order six-stage RK of Bogey and Bailly[5] (RK26–Bog) and the RK46–Ber. As soon as $|G(\omega\Delta t)|$ is greater than 1, the algorithm amplifies waves and becomes unstable. RK46–Ber and RK26–Bog are thus much more stable than the RK44 and the RK46–Sta. Stability limits are reported in Table 5. RK44 stability limit is about 2 time steps per period. RK26–Bog and RK46–Ber have a similar limit for about 1.6 time steps per period, which corresponds to $\omega\Delta t = 3.9$. RK46–Sta stability limit is closed to $\omega\Delta t = 1.7$, i.e. about 3.8 time steps per period. Limit of RK46–Ber is thus more than two times larger than this of the RK46–Sta.

The amount of dissipation $1 - |G(\omega\Delta t)|$ and the phase error $|\omega\Delta t - \omega^*\Delta t|/\pi$ are now represented in logarithmic scales in Figure 20 as a function of $\omega\Delta t$. RK44 is the most dissipative scheme with at least two orders of magnitude of difference compared to the RK26–Bog and RK46–Ber for $\omega\Delta t < \pi/2$. Dissipation improvement between RK46–Sta and RK26–Bog or RK46–Ber is about one order of magnitude for this range of pulsations. For higher pulsations, RK46–Sta is unstable. RK46–Ber and RK26–Bog have similar dissipation properties. The amount of dissipation is lower than 5×10^{-4} up to $\omega\Delta t = \pi/2$, i.e. for waves with four time steps per period.

Phase errors of the RK46–Sta, RK46–Ber and RK26–Bog remain similar for $\omega\Delta t < \pi/2$ and remain smaller than 5×10^{-4}. Compared to RK44 phase error improvement is for instance about one order of magnitude for $\omega\Delta t = \pi/3$. For $\omega\Delta t > \pi/2$, RK46–Sta has lower phase error than RK46–Ber and RK26–Bog, but for these pulsations the algorithm is unstable.

These results are quantitatively illustrated in Table 5 in terms of time steps per period. Two criteria of accuracy in amplitude and phase defined by Bogey[5] have been used: $1 - |G(\omega\Delta t)| < 5 \times 10^{-4}$ and $|\omega^*\Delta t - \omega\Delta t|/\pi < 5 \times 10^{-4}$. RK44 dissipation limit is about ten time steps per period and phase error limit is about eight time steps per period. Dissipation limit of the RK46–Sta is about five time steps per period, and phase error around three time steps per period. RK26–Bog and RK46–Ber have

dissipation limit of about three time steps per period and phase error limit close to four time steps per period. RK46–Ber is therefore able to accurately resolve at least four time-step-per-period waves.

Finally, in addition to the eight equations given by (36), linear optimization yields a new set of equations for the eleven coefficients $(\alpha_2, \ldots, \alpha_6, \beta_1, \ldots, \beta_6)$:

$$\begin{cases} \gamma_1 = \sum b_i \\ \gamma_2 = \sum b_i c_i \\ \gamma_3 = \sum b_i a_{ij} c_j \\ \gamma_4 = \sum b_i a_{ij} a_{jk} c_k \end{cases} \tag{44}$$

and,

$$\begin{cases} \gamma_5 = \sum b_i a_{ij} a_{jk} a_{kl} c_l \\ \gamma_6 = \sum b_i a_{ij} a_{jk} a_{kl} a_{lm} c_m \end{cases} \tag{45}$$

However, equations (44) on γ_1, γ_2, γ_3 and γ_4 are respectively similar to equations (O1).i, (O2).i, (O3).ii and (O4).iv of order conditions (36). Ten equations (eight order conditions and conditions on γ_5 and γ_6 given by linear optimization) are therefore found for the eleven coefficients $(\alpha_2, \ldots, \alpha_6, \beta_1, \ldots, \beta_6)$.

D. Nonlinear optimization

Since ten nonlinear equations are found for eleven unknowns, one parameter is free and must be imposed. Here to fix β_6, test problems have been solved for $0.14 \leq \beta_6 \leq 0.30$, this interval being the convergence interval of the Newton's iterations used to solve the set of nonlinear equations (36) and (45) which gives the α_i and β_i. The test cases are defined in appendix and the normalized errors are plotted in Figure 21 as functions of β_6. Accuracy according to β_6 is observed to depend on the test problem. For instance maximum accuracy is obtained for $\beta = 0.18$ with the case A_3 and for $\beta_6 = 0.30$ with the test case A_1. As a compromise, the value of $\beta_6 = 0.27$ is chosen. Coefficients of the Runge-Kutta scheme with $\beta = 0.27$, also referred to as RK46–Ber, are given in Table 17.

E. Test problems

To illustrate scheme properties, two test problems are solved: the linear convection of a wave packet with the 1D convective wave equation and the nonlinear propagation of Gaussian pressure pulse with the one-dimensional Euler equations.

Hence, the convective wave equation

$$\frac{\partial u}{\partial t} + \frac{\partial u}{\partial x} = 0 \tag{46}$$

is first solved, with a time step derived from the mesh spacing as $\Delta t = \mathrm{CFL} \cdot \Delta x$. Initial disturbances at $t = 0$ are defined as

$$u_0(x) = \cos\left(\frac{2\pi x}{a\Delta x}\right) \exp\left[-\ln(2)\left(\frac{x}{b\Delta x}\right)^2\right]$$

where $a\Delta x$ is the dominant wavelength and $b\Delta x$ the half-width of the Gaussian function. The parameters a and b are respectively set to $a = 6$ and $b = 12$. The initial disturbance and its normalized spatial power spectral density are then plotted in Figure 22. Spectral content is centered on a wave discretized with six points per wavelength, $k\Delta x = \pi/3$, and has a small width. Spatial derivation is computed with thirtieth-order thirty-one-point standard finite differences so that numerical errors due to derivative approximations are negligible compared to time integration errors.

The problem is solved for $0.1 < \mathrm{CFL} < 1.5$ up to $t = 100$ and the error rate is evaluated as

$$E_{num} = \frac{1}{N} \sum |u - u_e| \tag{47}$$

where u and u_e are respectively the computed and the exact solution, and N is the number of mesh points. Computed solutions for a CFL number of 1 are plotted in Figure 22 for RK44, RK26–Bog and RK46–Ber algorithms. RK44 solution is significantly dissipated, amplitude is indeed about sixty percent smaller. No significant dissipation nor dispersion is visible on solutions computed with the algorithms RK26–Bog and RK46–Ber.

The numerical error E_{num} is plotted in Figure 24 as a function of the CFL number. For CFL numbers lower than 0.7, error slope is driven by the order of accuracy. Second-order RK26–Bog has the smallest slope and thus its error decreases slower than the fourth-order algorithm RK44 and RK46–Ber as the CFL number decreases. For CFL numbers lower than 0.2, RK44 thus becomes more accurate than RK26–Bog. Over the interval $0.1 < \text{CFL} < 0.7$, RK46–Ber algorithm is the most accurate: improvement on accuracy is about one order of magnitude between RK46–Ber and RK44. Between RK46–Ber and RK26–Bog, error is similar at CFL = 0.7 whereas at CFL = 0.2 accuracy improvement is about one order of magnitude and is about two orders of magnitude at CFL = 0.1. For CFL numbers greater than 0.7, since the time step is large, Taylor series method failed to ensure accuracy and error is therefore given by the dissipation and dispersion properties of the scheme. RK44 error remains larger than those of RK46–Ber and RK26–Bog. RK26–Bog error decreases and becomes smaller than RK46–Ber error. RK26–Bog error reaches a minimum at CFL ~ 1.2. However, RK26–Bog and RK46–Ber error remain closed to each other over the interval $0.7 < \text{CFL} < 1.5$, difference is less than half an order of magnitude.

Actually, numerical errors of the test problem, where one frequency is dominant, change as the dispersion error of the RK algorithms. Indeed, consider Figure 20, where phase errors are plotted as functions of $\omega\Delta t$. As the numerical error, dispersion error of the RK46–Ber has a constant slope. In addition, according to the dispersion relation of the convective wave equation, $\omega = kc$, and thanks to the CFL number definition, $\text{CFL} = c\Delta t/\Delta x$, we may write that

$$\text{CFL} = \frac{k\Delta x}{\omega\Delta t} \tag{48}$$

where $k\Delta x = \pi/3$ for the present test problem. RK26–Bog dispersion error reaches a minimum at about $\omega\Delta t = 1.3$, i.e. around CFL = 1.2 as seen on the numerical error plot. Dissipation has also an influence on numerical errors. However, below $\omega\Delta t = \pi/2$, i.e. for CFL numbers lower than 1.5, dissipation properties are mainly driven by the order of accuracy so that no relevant change in error slope may be seen.

A nonlinear test problem is now considered, the one dimensional Euler equations:

$$\frac{\partial \mathbf{U}}{\partial t} + \frac{\partial \mathbf{E}}{\partial x} = 0 \tag{49}$$

where

$$\mathbf{U} = \begin{bmatrix} \rho \\ \rho u \\ \rho e_t \end{bmatrix} \quad , \qquad \mathbf{E} = \begin{bmatrix} \rho \\ \rho u^2 + p \\ u(\rho e_t + p) \end{bmatrix}$$

The total energy is given by

$$e_t = \frac{p}{\gamma - 1} + \frac{1}{2}\rho u^2 \tag{50}$$

Time integration is processed with the Runge-Kutta schemes. Spatial derivatives are computed with thirtieth-order thirty-one-point standard finite differences. Computation domain is taken large enough, 800 points, so that boundary conditions do not need to be implemented. No selective filtering is used. The equations are solved in dimensionless forms with $\Delta x = 1$ and $c = 1$.

The initial perturbation is a Gaussian pressure pulse at the center of the domain, with high amplitude to involve nonlinear propagation effects:

$$\begin{cases} \rho = 1 \\ u = 0 \\ p = \dfrac{1}{\gamma} + \Delta p\, e^{-\alpha x^2} \end{cases} \tag{51}$$

where $\gamma = 1.4$, $\alpha = 0.05$ and $\Delta p = 0.035$. It is propagated up to $t = 150$ for various CFL $= c\Delta x/\Delta t$ numbers. The solution computed for CFL $= 0.01$ is taken as the reference solution. Initial disturbance and reference solution are plotted in Figure 25. Wave front steepening due to nonlinear phenomena is clearly visible at $t = 150$. The error is computed as

$$E_{num} = \frac{1}{N} \sum |p - p_e| \tag{52}$$

where N is the number of mesh points and p_e the reference solution.

The numerical error E_{num} is plotted in Figure 26 as a function of the CFL number. As for the linear convection test case, the order of accuracy gives the slope of the error curve for CFL numbers lower than 0.7. RK44 error has thus a faster decrease than second-order RK26–Bog when the CFL number decreases. At CFL $= 0.2$ the two curves crossed each other and for lower CFL numbers RK44 is more accurate. RK46–Ber is the most precise for CFL numbers lower than 0.7. Precision difference is about two orders of magnitude at CFL $= 0.1$ between RK26–Bog and RK46–Ber, and one order of magnitude between RK44 and RK46–Ber.

When CFL number is higher than 0.7, error is no longer given by the order of accuracy. This part of the error curve is driven by dissipation and dispersion properties of the schemes: RK26–Bog becomes slightly more accurate than RK46–Ber. Contrary to the linear convection test problem, due to spectrum broadening by nonlinearities of the Euler equations, a large number of frequencies plays a role in generating numerical errors and no relevant minimum of the error is observed.

Finally, nonlinearities seem to have no significant influence on relative error between algorithms for the test case. Error is actually observed to be driven by the order of accuracy for low CFL numbers and by dissipation and dispersion properties for high CFL numbers. RK46–Ber is therefore accurate on both intervals thanks to its fourth order of accuracy and to linear optimization.

V. Conclusion

Explicit optimized algorithms have been proposed. First, high-order matching finite differences and selective filters permitting waves to travel from uniform Δx-mesh and uniform $2\Delta x$-mesh have been designed. Analysis of dispersion and dissipation properties and evaluation of accuracy limits demonstrate that these schemes resolve waves with at least five points per wavelength. They may be helpful for the computation of the acoustic far field generated by a turbulent flow. In addition, aerodynamic perturbations have been observed to generate low residual pressure as they pass through a mesh size change. Matching schemes could thus be used to elaborate a sponge zone. Non-centered schemes for boundary conditions have also been designed to resolve waves with at least five points per wavelength as shown by the investigation of dissipation and dispersion limits. A wall reflection test problem has highlighted the significant improvement of precision between centered and non-centered schemes. Finally, a fourth-order six-stage Runge-Kutta for time integration has been provided. The algorithm is stable at least for 1.6 time-step-per-period waves and resolves waves with at least four time steps per period. Linear and nonlinear propagation test cases have been solved to assess algorithm accuracy. It turns out that for low frequencies, precision of the time integration is ensured by accuracy of order four and for high frequencies, the algorithm is still accurate thanks to linear optimization.

Appendix – $\mathbf{A_i}$ test problems definition

Test problem $\mathbf{A_1}$ – nonlinear non-autonomous system of equations:

$$\begin{aligned} \frac{du}{dt} &= \frac{1}{u} - \frac{ve^{t^2}}{t^2} - t \\ \frac{dv}{dt} &= \frac{1}{v} - e^{t^2} - 2te^{-t^2} \end{aligned} \tag{53}$$

with the initial conditions $u(1) = 1$ et $v(1) = e^{-1}$. The exact solution is $u_e(t) = 1/t$ and $v_e(t) = e^{-t^2}$. The system is numerically solved for $t \in [1, 1.4]$ with $\Delta t = 0.1$. Error is defined as $E = |u - u_e| + |v - v_e|$ at $t = 1.4$.

Test problem $\mathbf{A_2}$ – simple equation:

$$\frac{du}{dt} = -u^{3/2} \tag{54}$$

for $t \in [0,1]$ with $u(0) = 1$ and $\Delta t = 0.05$. The exact solution is $u_e(t) = 1/\sqrt{1+t}$. Error is defined as $E = |u - u_e|$ at $t = 1$.

Test problem $\mathbf{A_3}$ – simple equation:

$$\frac{du}{dt} = u\,\cos(t) \tag{55}$$

for $t \in [0,1]$ with $u(0) = 1$ and $\Delta t = 0.05$. The exact solution is $u_e(t) = \exp(\sin(t))$. Error is defined $E = |u - u_e|$ at $t = 1$.

Test problem $\mathbf{A_4}$ – simple equation:

$$\frac{du}{dt} = u\frac{1 - u/20}{4} \tag{56}$$

for $t \in [0,1]$ with $u(0) = 1$ and $\Delta t = 0.05$. The exact solution is $u_e(t) = 20/\left(1 + 19\exp(-t/4)\right)$. Error is defined as $E = |u - u_e|$ at $t = 1$.

References

[1]Tam C.K.W. Computational aeroacoustics: issues and methods. *AIAA Journal*, **33**(10), 1788–1797, 1995.

[2]Hu F.Q., Hussaini M.Y. & Manthey J.L. Low-dissipation and low-dispersion Runge-Kutta schemes for computational acoustics. *J. Comput. Phys.*, **124**, 177–191, 1996.

[3]Lele S.K. Compact finite difference schemes with spectral-like resolution. *J. Comput. Phys.*, **103**, 16–42, 1992.

[4]Tam C.K.W. & Webb J.C. Dispersion-Relation-Preserving finite difference schemes for computational acoustics. *J. Comput. Phys.*, **107**, 262–281, 1993.

[5]Bogey C. & Bailly C. A family of low dispersive and low dissipative explicit schemes for flow noise and noise computations. *J. Comput. Phys.*, **194**, 194–214, 2003.

[6]Bogey C. & Bailly C. Direct computation of the sound radiated by a High-Reynolds number, subsonic round jet. CEAS Workshop From CFD to CAA, 7-8 November, NTUA, Athens, Greece, 2002.

[7]Bogey C. & Bailly C. LES of a high Reynolds, high subsonic jet: effects of the inflow conditions on flow and noise. *AIAA Paper 2003-3170*, 2003. See also *AIAA 2003-3557* & *AIAA 2004-3023*.

[8]Tam C.K.W. & Kurbatskii K.A. Multi-size-mesh multi-time-step dispersion-relation-preserving for multiple-scales aeroacoustics problems. *Int. J. Comp. Fluid Dyn.*, **17**(2), 119–132, 2003.

[9]Visbal M. R. & Gaitonde D.V. Higher-order-accurate methods for complex unsteady subsonic flows. *AIAA J.*, **37**(10), 1231–1239, 1999.

[10]Visbal M.R. Gaitonde D.V. Padé-type higher-order boundary filters for the Navier-Stokes equations. *AIAA Journal*, **38**(11), 2103–2112, 2000.

[11]Sherer S.E. & Visbal M.R. Computational study of acoustic scattering from multiple bodies using a high-order overset grid approach. *AIAA Paper*, (2003-3203), 2003.

[12]Visbal M.R., Morgan P.E. & Rizetta D.P. An implicit LES approach based on high-order compact differencing and filtering schemes (invited). *AIAA Paper*, (2003-4098), 2003.

[13]Tam C.K.W. & Dong Z. Wall boundary conditions or high-order finite-difference schemes in computational aeroacoustics. *Theoret. Comput. Fluid Dynamics*, **6**, 303–322, 1994.

[14]Williamson J.H. Low-storage Runge-Kutta schemes. *J. Comput. Phys.*, **35**, 48–56, 1980.

[15]Stanescu D. & Habashi W.G. 2N-storage low dissipation and dispersion Runge-Kutta schemes for computational acoustics. *J. Comput. Phys.*, **143**, 674–681, 1998.

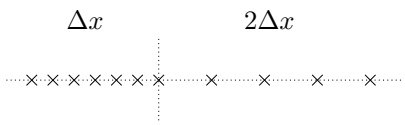

Figure 1: *Buffer region between Δx-mesh and $2\Delta x$-mesh.*

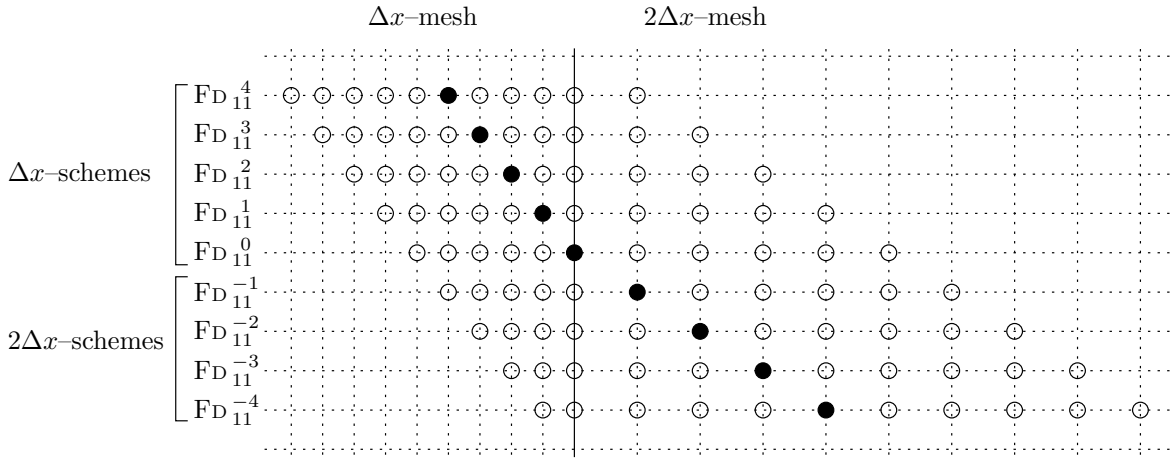

Figure 2: *Matching finite difference scheme stencils and names.*

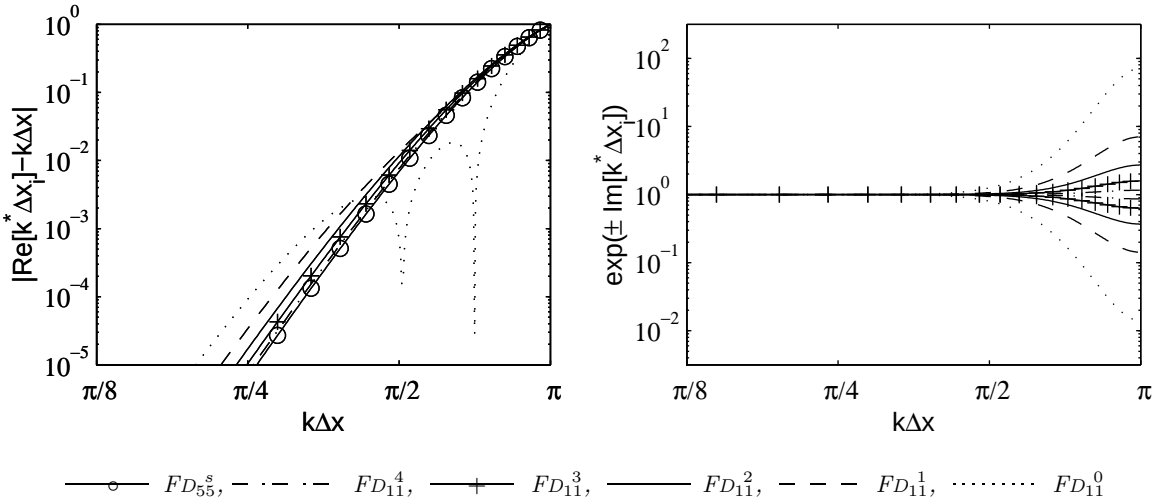

Figure 3: *Left: dispersion, and right: dissipation properties of the eleven-point matching Δx–schemes as functions of the wavenumber $k\Delta x$.*

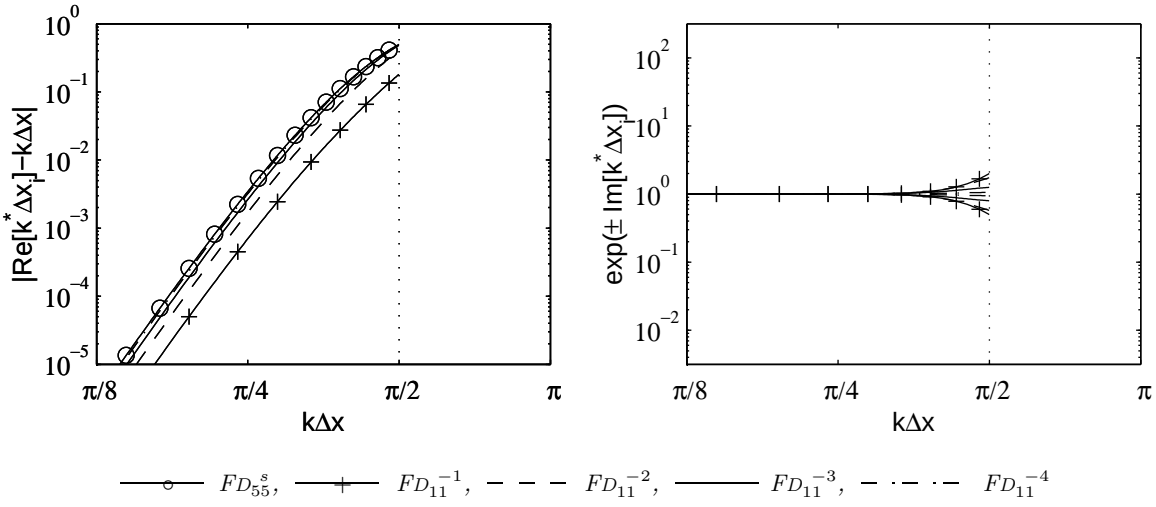

Figure 4: *Left: dissipation, and right: dispersion properties of the eleven-point matching $2\Delta x$–schemes as functions of the wavenumber $k\Delta x$. The dotted line shows the cut-off wavenumber of the scheme.*

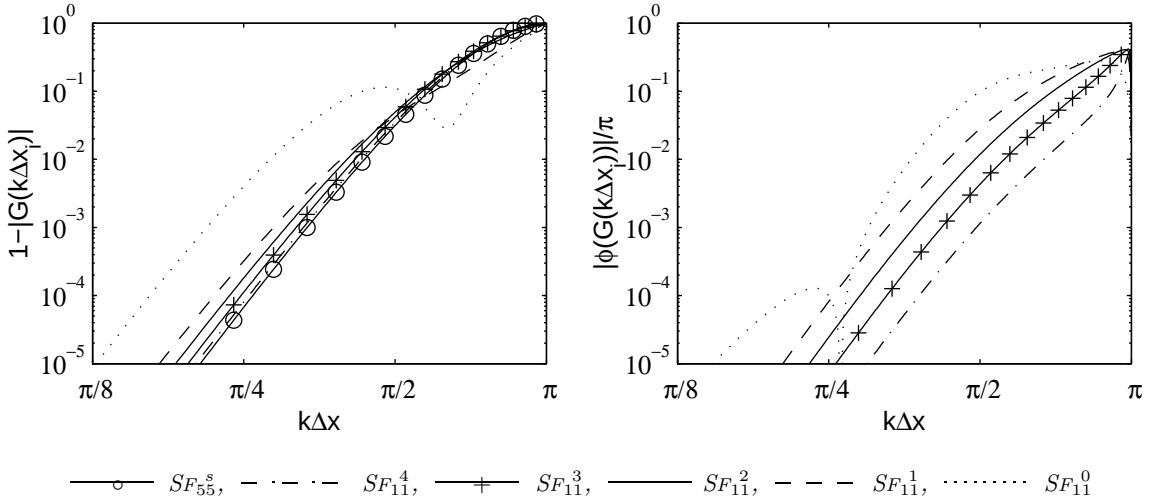

Figure 5: *Left: amplitude, and right: phase of the eleven-point matching Δx–selective filters as functions of the wavenumber $k\Delta x$.*

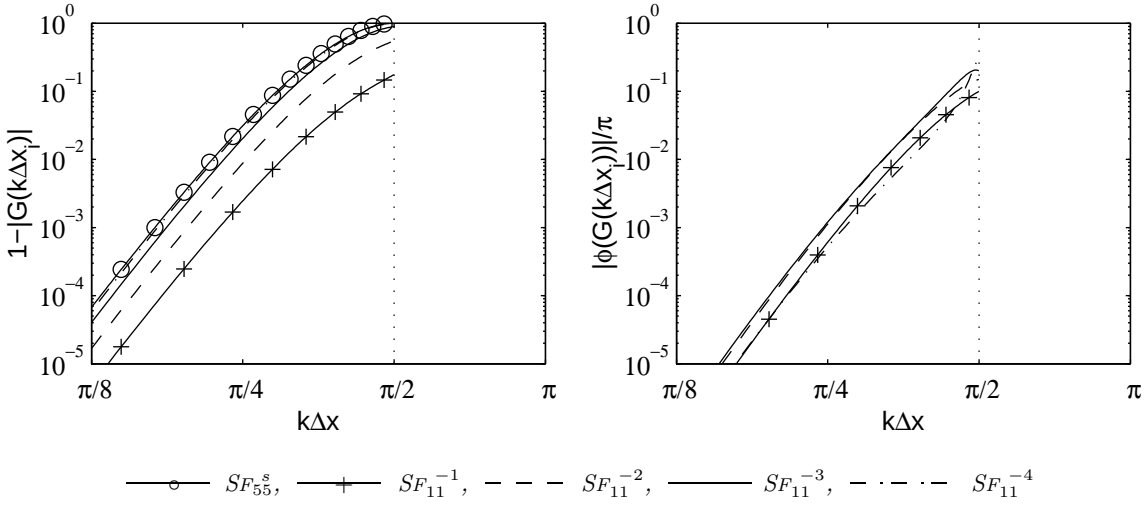

Figure 6: *Left: amplitude, and right: phase of the eleven-point matching $2\Delta x$–selective filters as functions of the wavenumber $k\Delta x$. The dotted line shows the cut-off wavenumber of the scheme.*

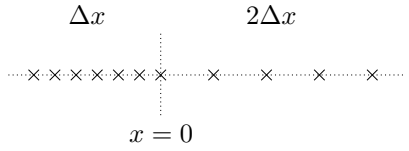

Figure 7: *Mesh size change for linear convection test problem.*

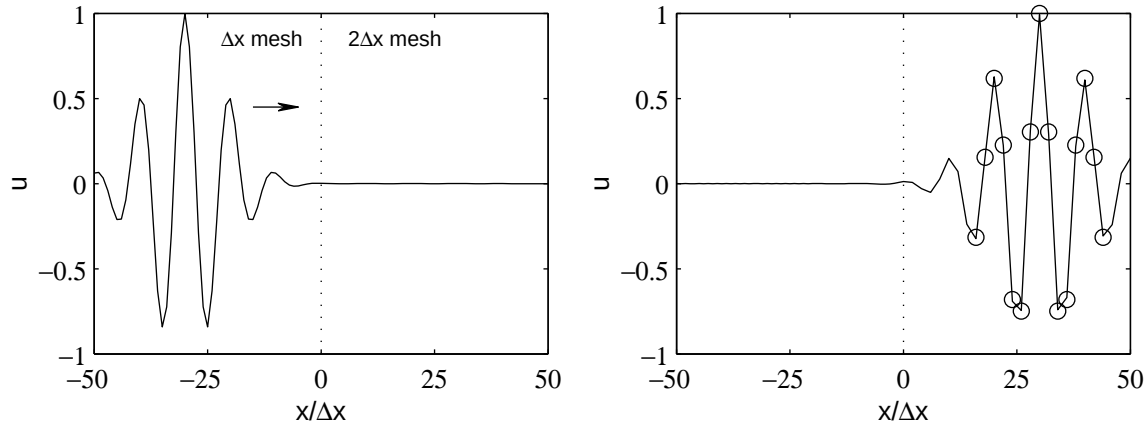

Figure 8: *Left: initial perturbation, and right: computed solution for the right-running wave (∘ exact solution). The arrow shows the propagation direction.*

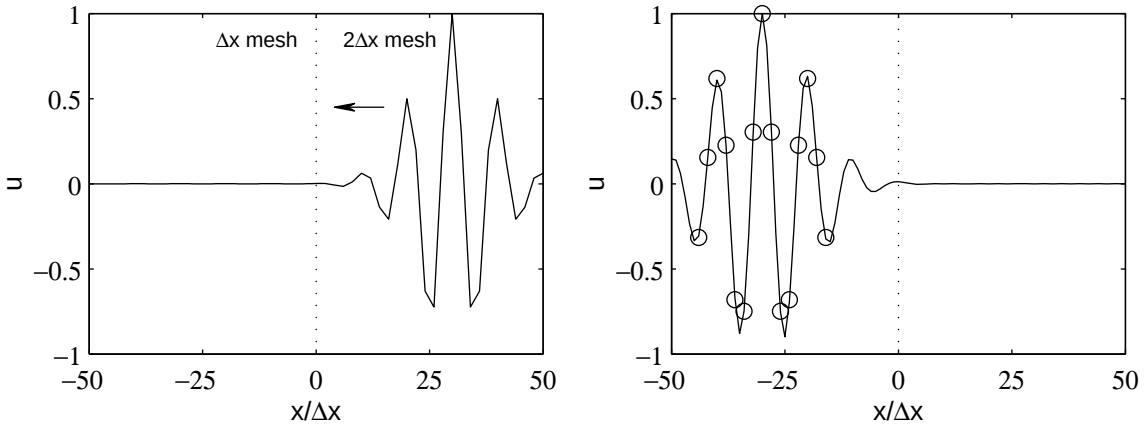

Figure 9: *Left: initial perturbation, and right: computed solution for the left-running wave (∘ exact solution). The arrow shows the propagation direction.*

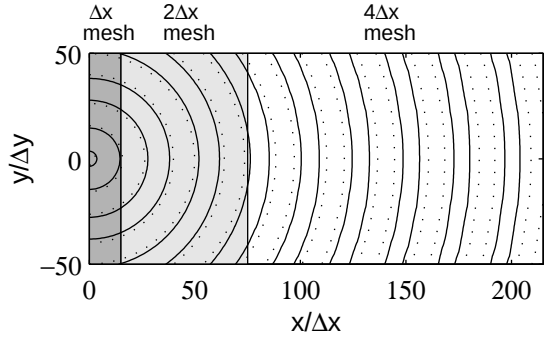

Figure 10: *Computed pressure for the acoustic source for $x \geq 0$. The gray stripe represents uniform mesh areas. Representation of iso-contours of pressure 0.99996×10^5 Pa and 1.00004×10^5 Pa.*

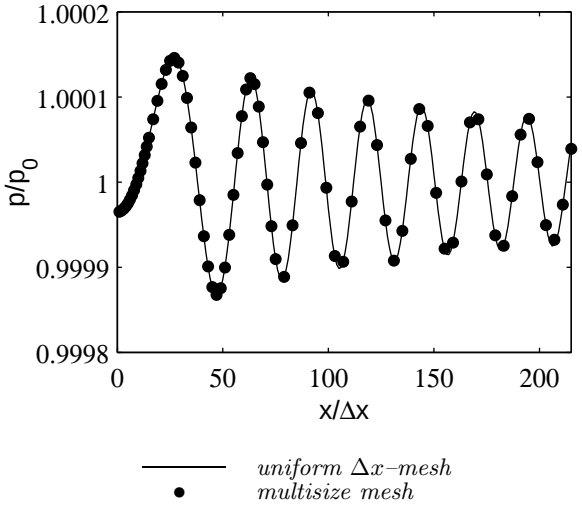

Figure 11: *Computed pressure for the acoustic source along the line $y = 0$ for the two mesh systems for $x \geq 0$.*

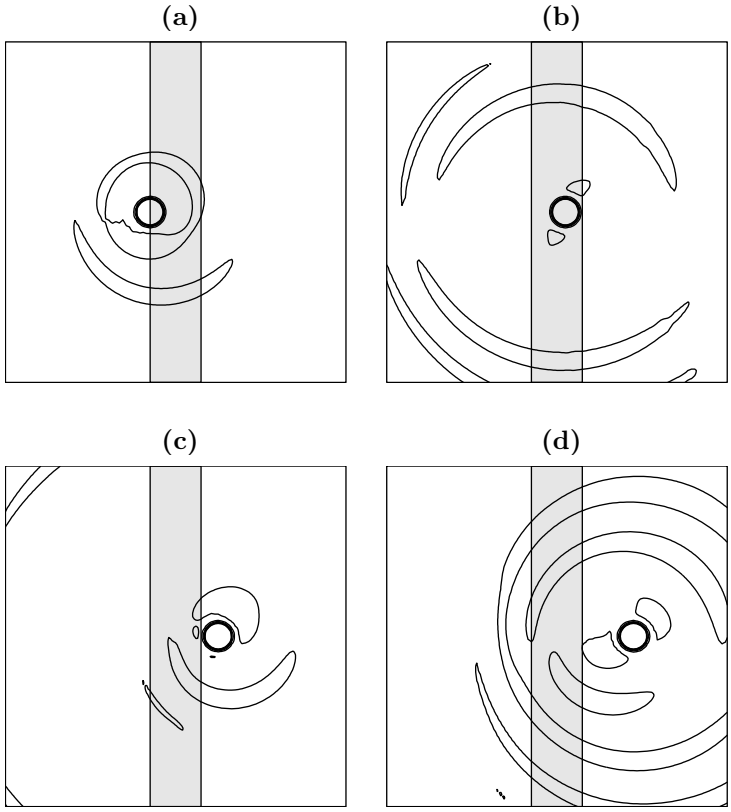

Figure 12: *Vortex in a uniform flow passing a finer mesh region. The gray stripe represents the Δx-mesh area. Representation of iso-contours of pressure from 0.9995×10^5 Pa to 1.0005×10^5 Pa by step of 1 Pa. (a) $t = t_0$. (b) $t = t_0 + 100\Delta t$. (c) $t = t_0 + 200\Delta t$. (d) $t = t_0 + 300\Delta t$.*

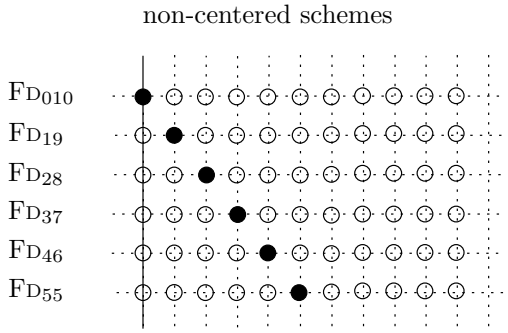

Figure 13: *Non-centered finite difference scheme stencils and names.*

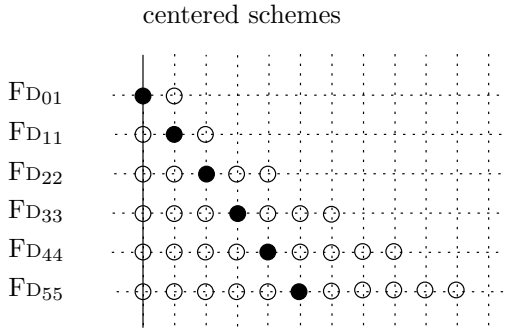

Figure 14: *Centered finite difference scheme stencils and names.*

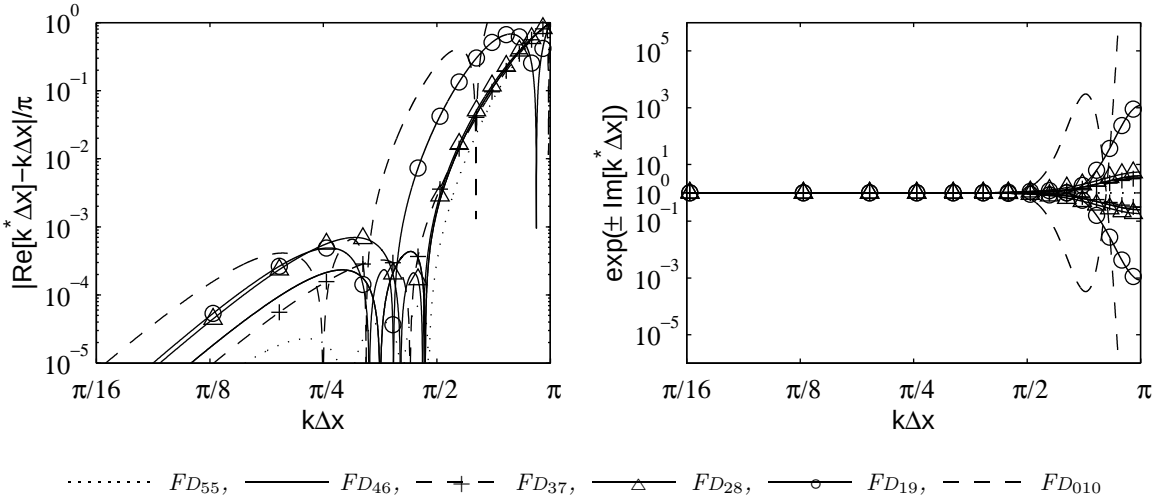

Figure 15: *Left: dispersion, and right: dissipation of the eleven-point boundary finite differences as functions of the wavenumber $k\Delta x$.*

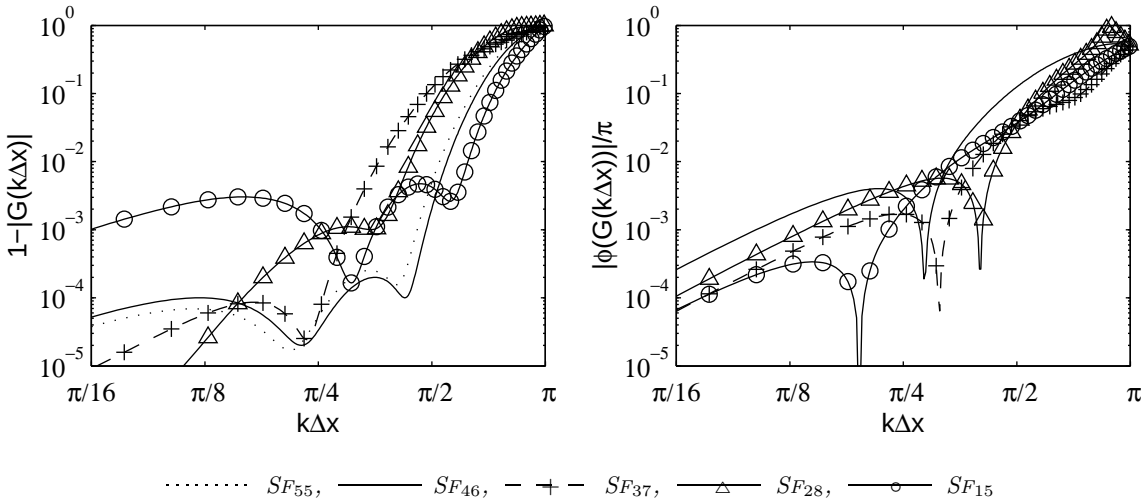

Figure 16: *Left: amplitude, and right: phase of the eleven-point boundary selective filters as functions of the wavenumber $k\Delta x$. Remark that SF_{15} is a seven points filter.*

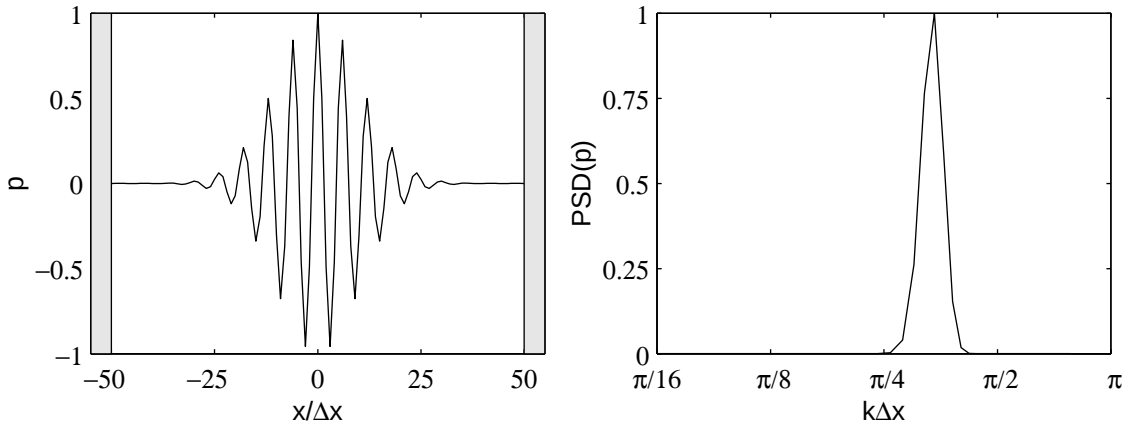

Figure 17: *Left: initial pressure perturbation, and right: initial spatial power spectral density for the acoustic problem. The gray stripes represents the wall boundaries.*

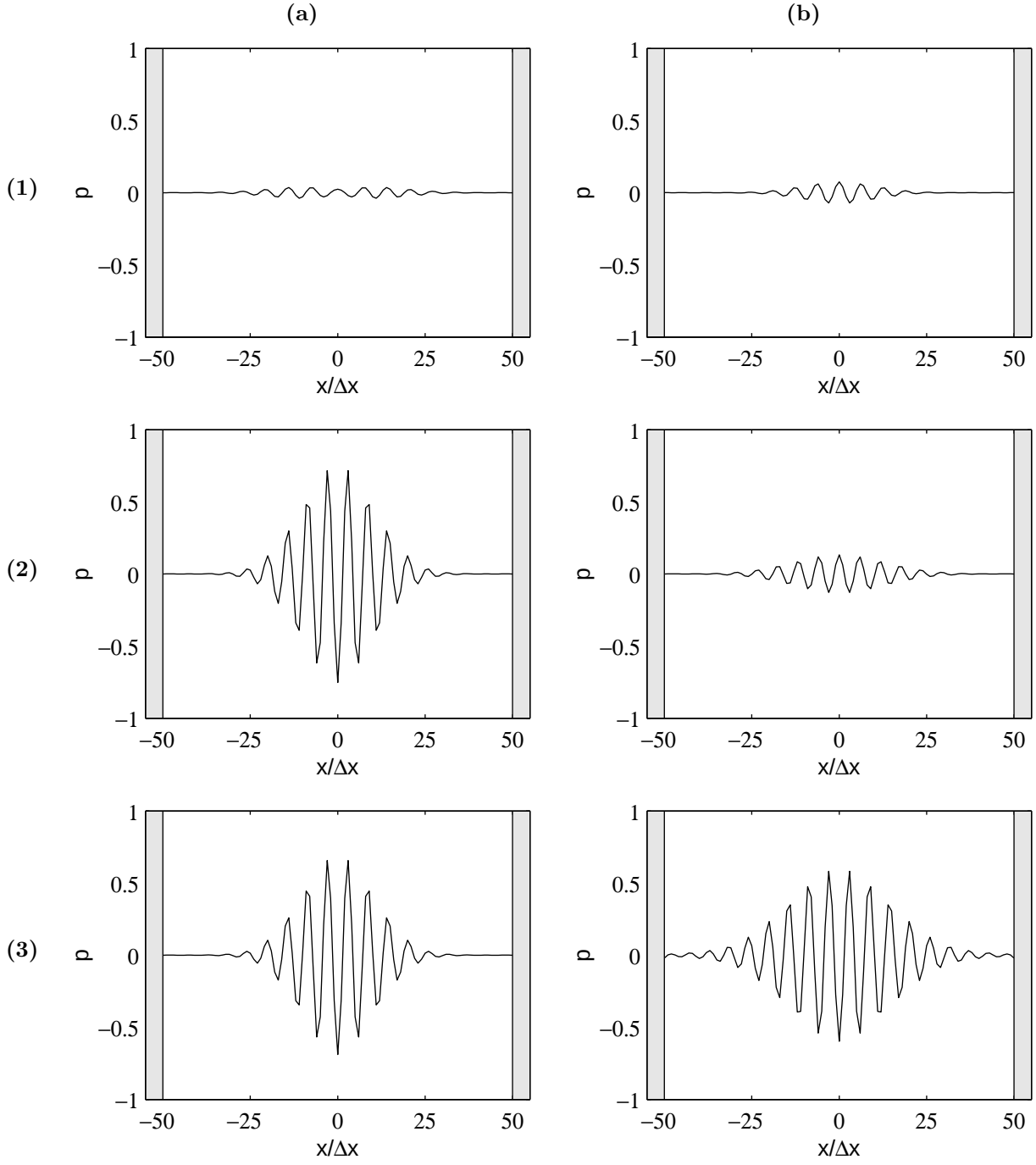

Figure 18: *Computed pressure for the acoustic test case. The gray stripes represents the wall boundaries. (a) $\sigma_d = 0.2$. (b) $\sigma_d = 0.8$. (1) centered finite differences, centered selective filters. (2) non-centered finite differences, centered selective filters. (3) non-centered finite differences, non-centered selective filters.*

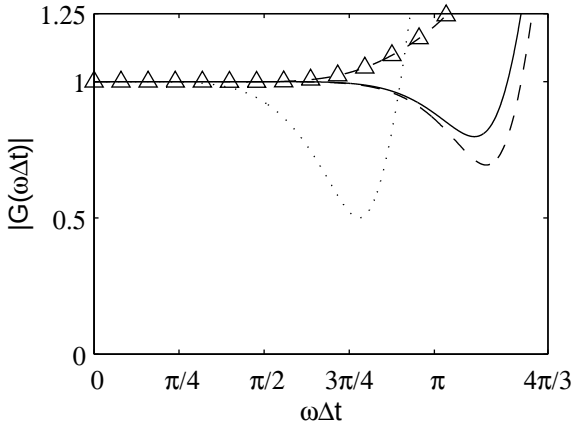

RK44: standard fourth-order four-stage Runge-Kutta
RK46–Sta: fourth-order four-stage Runge-Kutta developed by Stanescu and Habashi[15]
RK26–Bog: second-order six-stage Runge-Kutta of Bogey and Bailly[5]
RK46–Ber: fourth-order six-stage Runge-Kutta developed in the present work

Figure 19: *Amplification rate $|G(\omega\Delta t)|$ of the RK schemes as a function of the angular frequency $\omega\Delta t$.*

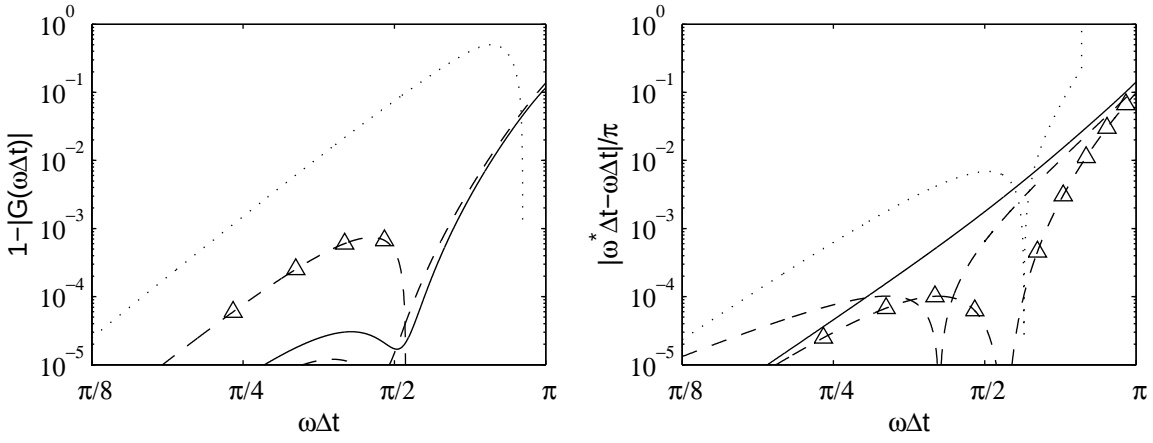

RK44: standard fourth-order four-stage Runge-Kutta
RK46–Sta: fourth-order four-stage Runge-Kutta developed by Stanescu and Habashi[15]
RK26–Bog: second-order six-stage Runge-Kutta of Bogey and Bailly[5]
RK46–Ber: fourth-order six-stage Runge-Kutta developed in the present work

Figure 20: *Left: dissipation, and right: phase error of the RK schemes as functions of the angular frequency $\omega\Delta t$.*

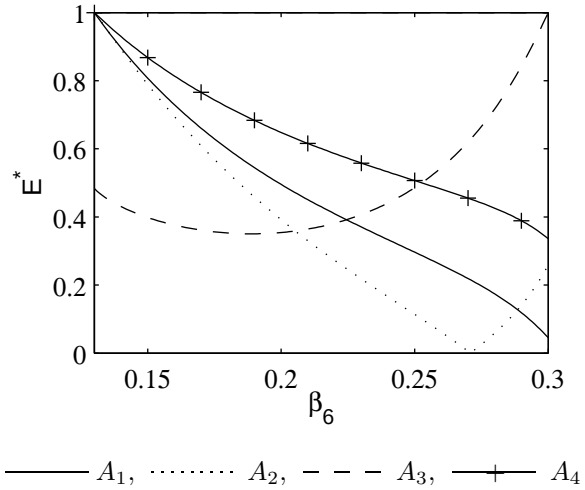

Figure 21: *Normalized error E^* as a function of β_6 for each test case.*

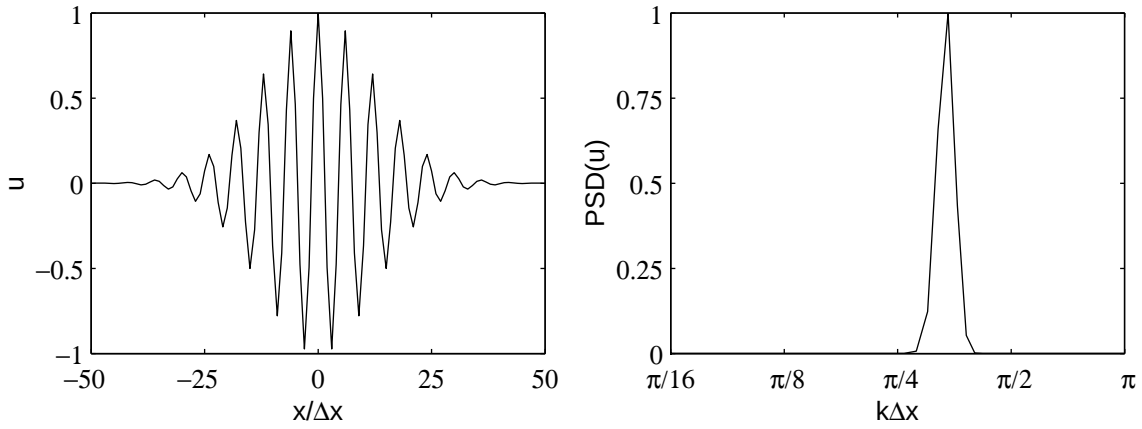

Figure 22: *Left: initial perturbation, and right: initial spatial power spectral density for the linear convection test problem.*

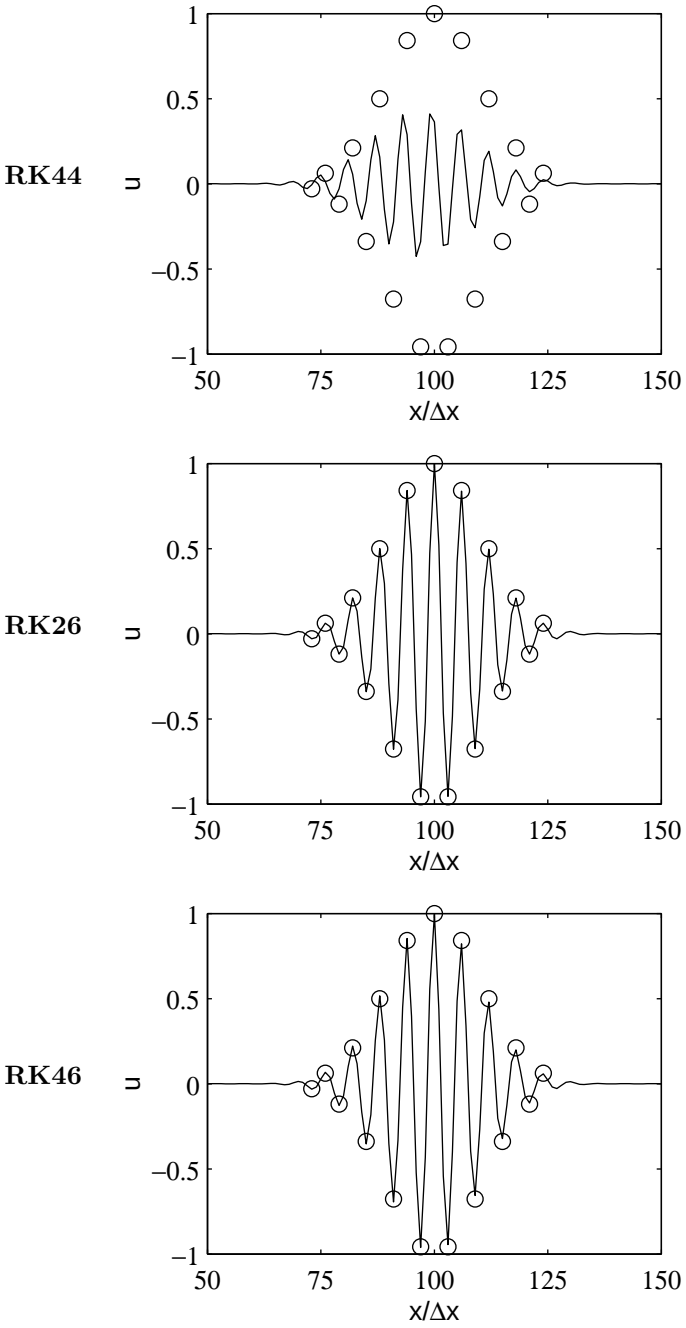

Figure 23: *Computed solutions at $t = 100$, for CFL $= 1$, for RK44, RK26–ber and RK46–Ber algorithms ($\circ$ exact solution).*

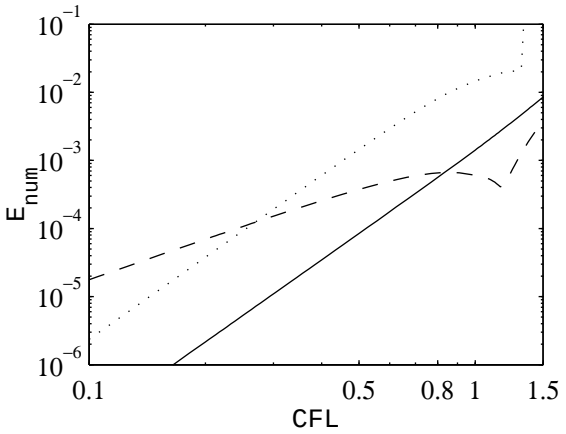

RK44: standard fourth-order four-stage Runge-Kutta
RK26–Bog: second-order six-stage Runge-Kutta of Bogey and Bailly[5]
RK46–Ber: fourth-order six-stage Runge-Kutta developed in the present work

Figure 24: *Linear convection error as a function of the CFL number for the Runge-Kutta schemes.*

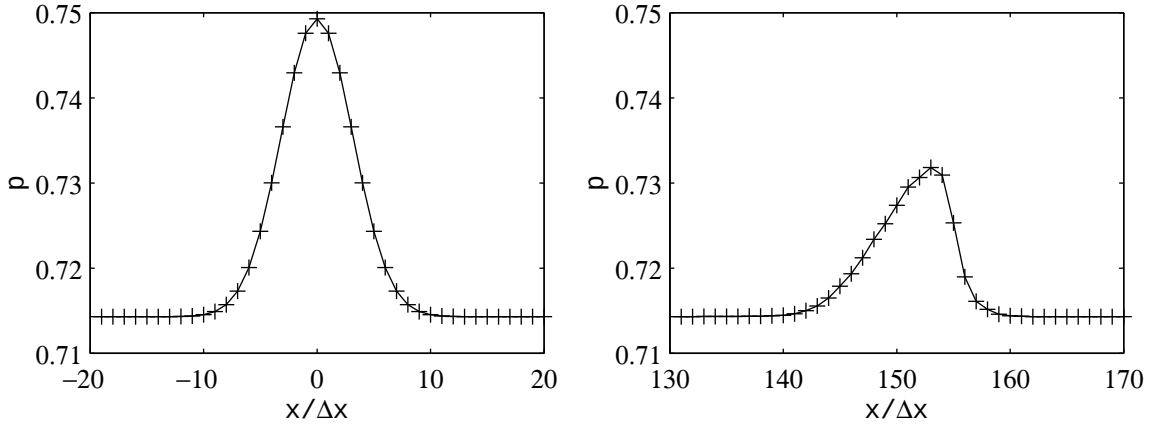

Figure 25: *Left: initial perturbation, and right: reference solution at* $t = 150$ *for the nonlinear propagation test case.*

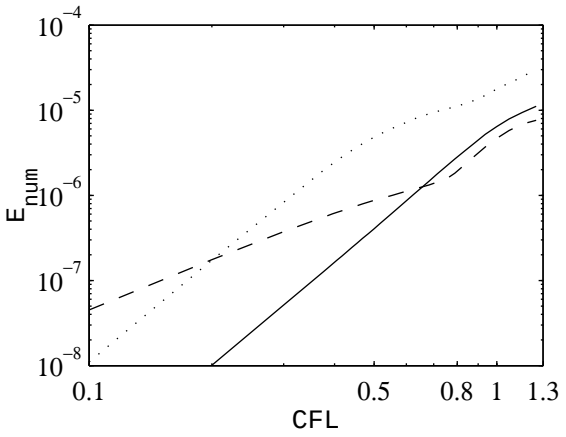

RK44: standard fourth-order four-stage Runge-Kutta
RK26–Bog: second-order six-stage Runge-Kutta of Bogey and Bailly[5]
RK46–Ber: fourth-order six-stage Runge-Kutta developed in the present work

Figure 26: *Nonlinear propagation error as a function of the CFL number for the Runge-Kutta schemes.*

Table 1: *Dispersion and dissipation limits of the eleven-point matching finite differences in wavenumber and in points per wavelength $\lambda/\Delta x = 2\pi/k\Delta x$ with respect to the Δx grid.*

	Dispersion $\lvert\mathcal{R}e(k^*\Delta x_i)-k\Delta x\rvert/\pi<5\times10^{-3}$		Dissipation $\lvert1-e^{\mathcal{I}m(k^*\Delta x_i)}\rvert<5\times10^{-3}$	
	$k\Delta x$	$\lambda/\Delta x$	$k\Delta x$	$\lambda/\Delta x$
$\mathrm{FD}_{55}^{s}{}_{/\Delta x}$	1.51	4.16	∞	0
FD_{11}^{4}	1.50	4.19	1.57	4.00
FD_{11}^{3}	1.46	4.30	1.48	4.25
FD_{11}^{2}	1.42	4.42	1.32	4.76
FD_{11}^{1}	1.37	4.59	1.17	5.37
FD_{11}^{0}	1.57	4.00	1.00	6.28
FD_{11}^{-1}	0.82	7.66	0.88	7.14
FD_{11}^{-2}	0.84	7.48	0.86	7.30
FD_{11}^{-3}	0.88	7.14	0.89	7.06
FD_{11}^{-4}	0.97	6.48	1.00	6.28
$\mathrm{FD}_{55}^{s}{}_{/2\Delta x}$	0.76	8.32	∞	0

Table 2: *Dissipation and phase error limits of the eleven-point matching selective filters in wavenumber and in points per wavelength $\lambda/\Delta x = 2\pi/k\Delta x$ with respect to the Δx grid.*

	Dissipation $1-\lvert G(k\Delta x_i)\rvert<5\times10^{-3}$		Phase error $\lvert\phi(G(k\Delta x_i))\rvert/\pi<5\times10^{-3}$	
	$k\Delta x$	$\lambda/\Delta x$	$k\Delta x$	$\lambda/\Delta x$
$\mathrm{SF}_{55}^{s}{}_{/\Delta x}$	1.25	5.03	∞	0
SF_{11}^{4}	1.23	5.11	1.57	4.00
SF_{11}^{3}	1.20	5.24	1.57	4.00
SF_{11}^{2}	1.15	5.46	1.40	4.49
SF_{11}^{1}	1.10	5.71	1.24	5.07
SF_{11}^{0}	0.80	7.85	1.07	5.87
SF_{11}^{-1}	0.85	7.40	0.99	6.34
SF_{11}^{-2}	0.73	8.60	0.93	6.76
SF_{11}^{-3}	0.66	9.52	0.92	6.82
SF_{11}^{-4}	0.63	9.98	1.04	6.04
$\mathrm{SF}_{55}^{s}{}_{/2\Delta x}$	0.63	9.98	∞	0

Table 3: *Dispersion and dissipation limits of the eleven-point boundary finite differences in wavenumber and in points per wavelength $\lambda/\Delta x = 2\pi/k\Delta x$.*

	Dispersion $\lvert\mathcal{R}e(k^*\Delta x)-k\Delta x\rvert/\pi<5\times10^{-3}$		Dissipation $\lvert1-e^{\mathcal{I}m(k^*\Delta x)}\rvert<5\times10^{-3}$	
	$k\Delta x$	$\lambda/\Delta x$	$k\Delta x$	$\lambda/\Delta x$
FD_{55}	1.79	3.51	∞	0
FD_{46}	1.67	3.77	1.41	4.46
FD_{37}	1.64	3.82	1.46	4.30
FD_{28}	1.65	3.81	1.19	5.28
FD_{19}	1.37	4.60	1.21	5.21
FD_{010}	1.13	5.59	1.38	4.56

Table 4: *Dissipation and phase error limits of the eleven-point boundary selective filters in wavenumber and in points per wavelength $\lambda/\Delta x = 2\pi/k\Delta x$.*

	Dissipation $1-\lvert G(k\Delta x)\rvert<5\times10^{-3}$		Phase error $\lvert\phi(G(k\Delta x))\rvert/\pi<5\times10^{-3}$	
	$k\Delta x$	$\lambda/\Delta x$	$k\Delta x$	$\lambda/\Delta x$
SF_{55}	1.57	4.00	∞	0
SF_{46}	1.64	3.83	0.98	6.41
SF_{37}	1.06	5.93	1.13	5.56
SF_{28}	1.30	4.83	1.33	4.72
SF_{15}	1.88	3.34	0.92	6.83

Table 5: *Stability, dissipation and dispersion limits of the Runge-Kutta schemes in time steps per period $T/\Delta t = 2\pi/\omega\Delta t$.*

	Stability $\lvert G(\omega\Delta t)\rvert<1$	Dissipation $1-\lvert G(\omega\Delta t)\rvert<5\times10^{-4}$	Dispersion $\lvert\omega^*\Delta t-\omega\Delta t\rvert/\pi<5\times10^{-4}$
RK44	2.22	9.65	8.40
RK46–Sta	3.80	5.32	3.13
RK26–Bog	1.59	3.29	5.03
RK46–Ber	1.65	3.19	4.10

Table 6: *Coefficients of the seven-point matching finite difference schemes.*

	$\mathrm{FD}_7{}^{2}$	$\mathrm{FD}_7{}^{1}$	$\mathrm{FD}_7{}^{0}$	$\mathrm{FD}_7{}^{-1}$	$\mathrm{FD}_7{}^{-2}$
a_{-3}	$\frac{-2}{105}$	$\frac{-5}{192}$	$\frac{-16}{315}$	$\frac{-3}{40}$	$\frac{-128}{3465}$
a_{-2}	$\frac{1}{6}$	$\frac{3}{14}$	$\frac{3}{8}$	$\frac{128}{315}$	$\frac{1}{8}$
a_{-1}	$\frac{-4}{5}$	$\frac{-15}{16}$	$\frac{-48}{35}$	$\frac{-3}{4}$	$\frac{-5}{12}$
a_0	$\frac{1}{12}$	$\frac{3}{10}$	$\frac{11}{12}$	$\frac{1}{6}$	$\frac{1}{30}$
a_1	$\frac{2}{3}$	$\frac{15}{32}$	$\frac{3}{20}$	$\frac{3}{10}$	$\frac{5}{14}$
a_2	$\frac{-1}{10}$	$\frac{-1}{48}$	$\frac{-3}{140}$	$\frac{-3}{56}$	$\frac{-5}{72}$
a_3	$\frac{1}{420}$	$\frac{3}{2240}$	$\frac{1}{504}$	$\frac{1}{180}$	$\frac{1}{132}$

Table 7: *Coefficients of the eleven-point matching finite difference schemes.*

	$\mathrm{FD}_{11}{}^{4}$	$\mathrm{FD}_{11}{}^{3}$	$\mathrm{FD}_{11}{}^{2}$	$\mathrm{FD}_{11}{}^{1}$	$\mathrm{FD}_{11}{}^{0}$	$\mathrm{FD}_{11}{}^{-1}$	$\mathrm{FD}_{11}{}^{-2}$	$\mathrm{FD}_{11}{}^{-3}$	$\mathrm{FD}_{11}{}^{-4}$
a_{-5}	$\frac{-1}{1155}$	$\frac{-1}{960}$	$\frac{-64}{45045}$	$\frac{-3}{1280}$	$\frac{-256}{45045}$	$\frac{-5}{336}$	$\frac{-2048}{153153}$	$\frac{-1}{144}$	$\frac{-32768}{14549535}$
a_{-4}	$\frac{3}{280}$	$\frac{5}{396}$	$\frac{1}{60}$	$\frac{15}{572}$	$\frac{5}{84}$	$\frac{2048}{15015}$	$\frac{5}{48}$	$\frac{32768}{765765}$	$\frac{1}{112}$
a_{-3}	$\frac{-4}{63}$	$\frac{-7}{96}$	$\frac{-64}{693}$	$\frac{-35}{256}$	$\frac{-2560}{9009}$	$\frac{-15}{28}$	$\frac{-2048}{6435}$	$\frac{-1}{12}$	$\frac{-1}{28}$
a_{-2}	$\frac{1}{4}$	$\frac{5}{18}$	$\frac{1}{3}$	$\frac{5}{11}$	$\frac{5}{6}$	$\frac{10240}{9009}$	$\frac{5}{12}$	$\frac{1}{6}$	$\frac{9}{70}$
a_{-1}	$\frac{-6}{7}$	$\frac{-175}{192}$	$\frac{-64}{63}$	$\frac{-315}{256}$	$\frac{-1280}{693}$	$\frac{-5}{4}$	$\frac{-7}{12}$	$\frac{-7}{15}$	$\frac{-3}{7}$
a_0	$\frac{1}{30}$	$\frac{3}{28}$	$\frac{29}{120}$	$\frac{125}{252}$	$\frac{137}{120}$	$\frac{37}{120}$	$\frac{33}{280}$	$\frac{3}{70}$	$\frac{1}{90}$
a_1	$\frac{4}{5}$	$\frac{35}{48}$	$\frac{64}{105}$	$\frac{105}{256}$	$\frac{5}{42}$	$\frac{15}{56}$	$\frac{25}{72}$	$\frac{7}{18}$	$\frac{9}{22}$
a_2	$\frac{-3}{14}$	$\frac{-1}{6}$	$\frac{-2}{21}$	$\frac{-5}{256}$	$\frac{-5}{252}$	$\frac{-5}{84}$	$\frac{-35}{396}$	$\frac{-7}{66}$	$\frac{-3}{26}$
a_3	$\frac{1}{21}$	$\frac{5}{192}$	$\frac{1}{252}$	$\frac{3}{1280}$	$\frac{5}{1386}$	$\frac{5}{396}$	$\frac{35}{1716}$	$\frac{1}{39}$	$\frac{1}{35}$
a_4	$\frac{-1}{168}$	$\frac{-1}{1440}$	$\frac{-1}{3465}$	$\frac{-5}{19712}$	$\frac{-5}{10296}$	$\frac{-15}{8008}$	$\frac{-1}{312}$	$\frac{-1}{240}$	$\frac{-9}{1904}$
a_5	$\frac{1}{13860}$	$\frac{1}{44352}$	$\frac{1}{72072}$	$\frac{5}{329472}$	$\frac{1}{30030}$	$\frac{1}{7280}$	$\frac{1}{4080}$	$\frac{1}{3060}$	$\frac{1}{2660}$

Table 8: *Coefficients of the seven-point matching finite selective filters.*

	$\mathrm{SF}_7{}^{2}$	$\mathrm{SF}_7{}^{1}$	$\mathrm{SF}_7{}^{0}$	$\mathrm{SF}_7{}^{-1}$	$\mathrm{SF}_7{}^{-2}$
d_{-3}	$\frac{-3}{161}$	$\frac{-35}{1336}$	$\frac{-32}{771}$	$\frac{-9}{146}$	$\frac{-4}{77}$
d_{-2}	$\frac{5}{46}$	$\frac{24}{167}$	$\frac{128}{511}$	$\frac{128}{511}$	$\frac{9}{64}$
d_{-1}	$\frac{-6}{23}$	$\frac{-105}{334}$	$\frac{-45}{146}$	$\frac{-45}{146}$	$\frac{-15}{64}$
d_0	$\frac{15}{46}$	$\frac{56}{167}$	$\frac{15}{73}$	$\frac{15}{73}$	$\frac{9}{32}$
d_1	$\frac{-5}{23}$	$\frac{-105}{668}$	$\frac{-9}{73}$	$\frac{-9}{73}$	$\frac{-45}{224}$
d_2	$\frac{3}{46}$	$\frac{7}{334}$	$\frac{45}{1022}$	$\frac{45}{1022}$	$\frac{5}{64}$
d_3	$\frac{-1}{322}$	$\frac{-3}{1336}$	$\frac{-1}{146}$	$\frac{-1}{146}$	$\frac{-9}{704}$

Table 9: *Coefficients of the eleven-point matching selective filters.*

	$\mathrm{SF}_{11}{}^{4}$	$\mathrm{SF}_{11}{}^{3}$	$\mathrm{SF}_{11}{}^{2}$	$\mathrm{SF}_{11}{}^{1}$	$\mathrm{SF}_{11}{}^{0}$	$\mathrm{SF}_{11}{}^{-1}$	$\mathrm{SF}_{11}{}^{-2}$	$\mathrm{SF}_{11}{}^{-3}$	$\mathrm{SF}_{11}{}^{-4}$
d_{-5}	$\frac{-5}{4609}$	$\frac{-33}{24620}$	$\frac{-10}{5421}$	$\frac{-429}{151876}$	0.000638963653	$\frac{-2145}{256816}$	$\frac{-3072}{365041}$	$\frac{-1105}{96418}$	$\frac{-64}{13167}$
d_{-4}	$\frac{9}{838}$	$\frac{16}{1231}$	$\frac{77}{4448}$	$\frac{960}{37696}$	0.006919771220	$\frac{1024}{16051}$	$\frac{2145}{42946}$	$\frac{32768}{530299}$	$\frac{1105}{64512}$
d_{-3}	$\frac{-20}{419}$	$\frac{-693}{12310}$	$\frac{-10}{139}$	$\frac{-15015}{151876}$	-0.068720278343	$\frac{-6435}{32102}$	$\frac{-2048}{21473}$	$\frac{-9945}{96418}$	$\frac{-1105}{21504}$
d_{-2}	$\frac{105}{838}$	$\frac{176}{1231}$	$\frac{385}{2224}$	$\frac{8320}{37969}$	0.220268627322	$\frac{5120}{16051}$	$\frac{5120}{21473}$	$\frac{6630}{48209}$	$\frac{221}{1792}$
d_{-1}	$\frac{-90}{419}$	$\frac{-1155}{4924}$	$\frac{-110}{417}$	$\frac{-45045}{151876}$	-0.339320510296	$\frac{-2145}{9172}$	$\frac{-6006}{21473}$	$\frac{-1326}{6887}$	$\frac{-1105}{5376}$
d_0	$\frac{105}{419}$	$\frac{1584}{6155}$	$\frac{1155}{4448}$	$\frac{9152}{37969}$	0.235259313661	$\frac{429}{4586}$	$\frac{3432}{21473}$	$\frac{9945}{48209}$	$\frac{1105}{4608}$
d_1	$\frac{-84}{419}$	$\frac{-231}{1231}$	$\frac{-22}{139}$	$\frac{-15015}{151876}$	-0.080561297840	$\frac{-6435}{128408}$	$\frac{-2145}{21473}$	$\frac{-1105}{6887}$	$\frac{-1105}{5632}$
d_2	$\frac{45}{419}$	$\frac{528}{6155}$	$\frac{55}{1112}$	$\frac{2145}{151876}$	0.035036157793	$\frac{715}{32102}$	$\frac{1040}{21473}$	$\frac{6630}{75757}$	$\frac{85}{768}$
d_3	$\frac{-15}{419}$	$\frac{-99}{4924}$	$\frac{-55}{13344}$	$\frac{-429}{151876}$	-0.011786877175	$\frac{-65}{9172}$	$\frac{-350}{21473}$	$\frac{-1530}{48209}$	$\frac{-221}{5376}$
d_4	$\frac{5}{838}$	$\frac{11}{12310}$	$\frac{1}{2224}$	$\frac{65}{151876}$	0.002516130003	$\frac{45}{32102}$	$\frac{72}{21473}$	$\frac{663}{96418}$	$\frac{65}{7168}$
d_5	$\frac{-1}{9218}$	$\frac{-1}{24620}$	$\frac{-5}{173472}$	$\frac{-5}{151876}$	-0.00025	$\frac{-33}{256816}$	$\frac{-231}{730082}$	$\frac{-65}{96418}$	$\frac{-1105}{1225728}$

Table 10: *Coefficients of the seven-point non-centered finite differences.*

	FD_{24}	FD_{15}	FD_{06}
a_{-2}	0.040608484938		
a_{-1}	-0.439403255112	-0.212932721951	
a_0	-0.495444331840	-1.060320390770	-2.221732927347
a_1	1.230306846391	2.078926116439	4.792392499971
a_2	-0.433349271080	-1.287179452384	-4.885968589653
a_3	0.110920696280	0.685176395471	3.721274572504
a_4	-0.013639169577	-0.245320613994	-1.945943269102
a_5		0.041650667189	0.640372243531
a_6			-0.100394529903

Table 11: *Coefficients of the eleven-point non-centered finite differences.*

i	FD_{46}	FD_{37}	FD_{28}	FD_{19}	FD_{010}
a_{-4}	0.016756572303				
a_{-3}	-0.117478455239	-0.013277273810			
a_{-2}	0.411034935097	0.115976072920	0.046246319744		
a_{-1}	-1.130286765151	-0.617479187931	-0.462989982072	-0.180022054228	
a_0	0.341435872100	-0.274113948206	-0.459203180244	-1.237550583044	-2.391602219538
a_1	0.556396830543	1.086208764655	1.205900619436	2.484731692990	5.832490322294
a_2	-0.082525734207	-0.402951626982	-0.423956587692	-1.810320814061	-7.650218001182
a_3	0.003565834658	0.131066986242	0.102329382027	1.112990048440	7.907810563576
a_4	0.001173034777	-0.028154858354	-0.006253229685	-0.481086916514	-5.922599052629
a_5	-0.000071772607	0.002596328316	-0.002025942780	0.126598690230	3.071037015445
a_6	-0.000000352272	0.000128743150	-0.000016793609	-0.015510730165	-1.014956769726
a_7		0	-0.000015302561	0.000021609059	0.170022256519
a_8			-0.000015302561	0.000156447571	0.002819958377
a_9				-0.000007390277	-0.004791009708
a_{10}					-0.000013063429

Table 12: *Coefficients of the seven-point non-centered selective filters.*

	SF_{24}	SF_{15}
d_{-2}	0.032649010764	
d_{-1}	-0.143339502575	-0.057717512738
d_0	0.273321177980	0.199278374994
d_1	-0.294622121167	-0.292668277650
d_2	0.186711738069	0.244537361546
d_3	-0.062038376258	-0.134605018019
d_4	0.007318073189	0.056184263460
d_5		-0.015009191593

Table 13: *Coefficients of the eleven-point non-centered selective filters.*

i	SF_{46}	SF_{37}	SF_{28}
d_{-4}	0.009095822490		
d_{-3}	0.013892091123	-0.000054596010	
d_{-2}	-0.060031967800	0.042124772446	0.052523901012
d_{-1}	-0.061297562648	-0.173103107841	-0.206299133811
d_0	0.356344029930	0.299615871352	0.353527998250
d_1	-0.488142768372	-0.276543612935	-0.348142394842
d_2	0.276991103162	0.131223506571	0.181481803619
d_3	0.002551524249	-0.023424966418	0.009440804370
d_4	-0.076307201417	0.013937561779	-0.077675100452
d_5	0.032996715648	-0.024565095706	0.044887364863
d_6	-0.006091786366	0.013098287852	-0.009971961849
d_7		-0.002308621090	0.000113359420
d_8			0.000113359420
d_9			

Table 14: *Coefficients and order of accuracy of the centered standard finite differences.*

	FD_{01} 1th-order	FD_{11} 2nd-order	FD_{22} 4th-order	FD_{33} 6th-order	FD_{44} 8th-order
a_{-4}					1/280
a_{-3}				-1/60	-4/105
a_{-2}			1/12	3/20	1/5
a_{-1}		-1/2	-2/3	-3/4	-4/5
a_0	-1	0	0	0	0
a_1	1	1/2	2/3	3/4	4/5
a_2			-1/12	-3/20	-1/5
a_3				1/60	4/105
a_4					-1/280

Table 15: *Coefficients and order of accuracy of the centered standard selective filters.*

	SF_{11} 2nd-order	SF_{22} 4th-order	SF_{33} 6th-order	SF_{44} 8th-order
d_{-4}				1/256
d_{-3}			-1/64	-1/32
d_{-2}		1/16	3/32	7/64
d_{-1}	-1/4	-1/4	-15/64	-7/32
d_0	1/2	3/8	5/16	35/128
d_1	-1/4	-1/4	-15/64	-7/32
d_2		1/16	3/32	7/64
d_3			-1/64	-1/32
d_4				1/256

Table 16: γ_j *coefficients of the RK46–Ber scheme.*

γ_1	1
γ_2	1/2
γ_3	1/6
γ_4	1/24
γ_5	0.007856772044
γ_6	0.000959998595

Table 17: *Coefficients of the RK46–Ber scheme.*

i	α	β	c
1	0.0	0.032918605146	0.0
2	-0.737101392796	0.823256998199	0.032918605146
3	-1.634740794341	0.381530948900	0.249351723343
4	-0.744739003780	0.200092213184	0.466911705055
5	-1.469897351522	1.718581042715	0.582030414044
6	-2.813971388035	0.27	0.847252983783